

**Pore-scale Mechanisms of Two-phase Flow in Porous Materials;**

Volume-of-Fluid Method and Pore-network Modelling

**Porieschaal Mechanismen van Tweefasenstroming in Poreuze Materialen;**

Volume-van-Vloeistof Methode en Porienetwerk Modelling

(met een samenvatting in het Nederlands)

**PROEFSCHRIFT**

ter verkrijging van de graad van doctor aan de Universiteit Utrecht op gezag van de rector magnificus, prof. dr. G.J. van der Zwaan, ingevolge het besluit van het college voor promoties in het openbaar te verdedigen op vrijdag 23 februari 2018 des ochtends te 10.30 uur

door

**Xiaoguang Yin**

geboren in 1988 te Yantai, China

Promotor: Prof.dr.ir. S.M. Hassanizadeh

Copromotor: Dr. A. Raof

This thesis was accomplished with financial support from the China Scholarship Council (CSC).

This thesis is dedicated to my grandma, who has been unconscious for months and cannot recognize her grandson any more.



**Pore-scale Mechanisms of Two-phase Flow in Porous Materials;**

Volume-of-Fluid Method and Pore-network Modelling

**Xiaoguang Yin**

**The Reading Committee**

Prof. A. Hansen

Norwegian University of Science and Technology

Prof. Celia, M. A.

Princeton University

Prof. R. Helmig

Stuttgart University

Prof. V. Cnudde

University of Gent

Dr. Niasar, V.J.

The University of Manchester

Copyright ©2018 by Xiaoguang Yin

All rights reserved. No part of this material may be copied or reproduced in any way without the prior permission of the author.

---

ISBN: 978-90-6266-501-3

Title: Pore-scale mechanisms of two-phase flow in porous materials; Volume-of-Fluid method and pore-network modelling

NUR-code: 934

NUR-description: Hydrogeology

Number of pages: 91

Printed by: ProefschriftMaken || [www.proefschriftmaken.nl](http://www.proefschriftmaken.nl)

---

## Acknowledgements

I have to thank the four years time, during which I could start my PhD research, join the wonderful group, know reputed scholars in the field, get acquainted with new friends and lucky enough to encounter my girlfriend. I would like to express my thanks to all these that have made my research and life easier and colourful.

First of all, my greatest gratitude goes to my supervisor, Majid Hassanizadeh, without whom my PhD study would have been impossible. I still remember the first time he introduced me mechanics and thermodynamics of discontinuous phases, a field that I have never thought of, in a way that I could not have imagined. Although our work on discontinuous phases did not work well, I did develop my feeling of the topic and tastes for research. Four years is a long journey not only for me, but also for the supervisor. His guidance, encouragement, criticism throughout the journey led me out and will continue to lead me in the future work. Majid, thank you in all aspects!

I wish to thank my co-supervisor, Amir Raoof. I did enjoy the time discussing with him about algorithms of pore-network modelling and optimizations of the algorithms. His patient correcting improved my writings a lot.

I am grateful to Nikolaos K. Karadimitriou of *Manchester University* for explaining a lot about his experimental set up and micromodel experiments. Thanks to Vahid J. Niasar of *Manchester University* for discussions on pore-network modeling. Many thanks to Ioannis for patiently conducting a number of experiments when we tried to figure out discrepancies between simulations and experimental measurements. Thanks to Enno for optimizing the pore-network code. Thanks to Hamed for efforts and time on paper coating layer work. I learned a lot from talks with Philip Kuns from *University of Stuttgart* when we simulated the same micromodel experiment using different methods. Thank Prof. Jeannot Trampert and Theo van Zessen of seismology group in *Utrecht University* for kindly allowing me access to cluster grit.

I thank the inspiring discussions with Mike Celia from *Princeton University*, Rainer Helmig from *University of Stuttgart*, Rien van Genuchten, Jan Martin Nordbotten from

*Bergen University* and Sorin Pop from *University of Hasselt* at conferences/workshops or during their stay in Utrecht.

My personality changed a lot thanks to the nice colleagues and friendly atmosphere of the group here in Utrecht. I must thank Margreet and Annuska for the administrative work. I want to thank my roommates Mojtaba, Jan and Gillian for nice daily office life. I also want to thank Thomas for sunny lunch walks. I also would like to thank the other colleagues and friends: Ruud Schotting, Jack Schijven, Niels Hartog, Willem-Bart, Pierre, Ehsan, Lucas, Amir, Arjen, Sayantan, and Galip for cheerful coffee chats, great Friday drinks and delicious birthday cakes.

I need to thank the Chinese colleagues and friends in the group: Chaozhong, I benefited a lot from discussions with you; Qiulan, thanks for helping me settling down when I just arrived in Utrecht; Shuai, thanks for the nice food and teaching me how to cook; and Luwen, thanks for joyful food time talks and for inviting me to the festival dinners to know your friends.

I want to thank the accompany of my housemates over the years: Jieying, Rui, Qinwei, Shengmei, Wenbin, Feijia, Peiyuan, Ye, Yidi, and Zhihan, thank you all for the great living environment. Many thanks to Jinfeng, Jiawang, Xiaochen, Xue, Jingchao, Miao, Shaohui, Xiulei, and Chunhui.

I also want to thank my friends since college days: Zeyong, Jing and Zhihua, thank their hospitality during my travel in US and their encouragements over the years on PhD study and life.

I have to thank Xusong, my friend since high school, for accommodating me during my stay in Beijing finding a position.

I want to thank my girlfriend Zhenpei for her understanding, support and comforting.

Last but not least, I should thank my parents and our big family, your support, encouragement and love teaches me the truth, the goodness and the beauty.

# Table of contents

<b>1</b>	<b>Introduction</b>	<b>1</b>
1.1	Benchmarking Volume-of-Fluid method . . . . .	1
1.2	Pore-network modeling . . . . .	3
1.3	Thesis outline . . . . .	4
<b>2</b>	<b>Direct Simulations of Two-phase Flow Experiments Using Volume-of-Fluid (VOF) Method</b>	<b>5</b>
2.1	Introduction . . . . .	7
2.2	Numerical model description . . . . .	9
2.2.1	Description of VOF method . . . . .	9
2.2.2	Corrected-two-dimensional model . . . . .	11
2.3	Experiments simulated in this study . . . . .	11
2.3.1	Capillary rise experiment . . . . .	11
2.3.2	Micromodel experiments . . . . .	12
2.4	Simulation results and discussion . . . . .	14
2.4.1	Verification of corrected-two-dimensional model . . . . .	14
2.4.2	Capillary rise experiment . . . . .	15
2.4.3	Micromodel experiments . . . . .	15
2.4.4	Discussions . . . . .	18
2.5	Summary and Conclusion . . . . .	19
<b>3</b>	<b>Dynamic Pore-network Models Development</b>	<b>21</b>
3.1	Introduction . . . . .	23
3.2	Pore-network model description . . . . .	25
3.2.1	Model features . . . . .	25
3.2.2	local rules . . . . .	27
3.2.3	Governing equations . . . . .	30

3.2.4	Time step . . . . .	33
3.2.5	Computational procedure . . . . .	34
3.3	Simulations and discussions . . . . .	35
3.3.1	Boundary conditions . . . . .	35
3.3.2	Averaging procedure . . . . .	35
3.3.3	Two-pressure drainage simulations . . . . .	35
3.3.4	Single-pressure imbibition: flow pattern for different boundary pressure drop . . . . .	39
3.4	Conclusion . . . . .	39
<b>4</b>	<b>Droplet Imbibition into Paper Coating Layer: Pore-network Modeling</b>	
	<b>Simulations</b> . . . . .	<b>43</b>
4.1	Introduction . . . . .	45
4.2	Properties of paper coating layer . . . . .	48
4.2.1	Properties based on FIB-SEM image . . . . .	48
4.3	Pore-network model description . . . . .	49
4.3.1	Model features . . . . .	49
4.4	Dynamic simulation results and discussion . . . . .	50
4.4.1	Symmetry of saturation pattern during droplet penetration . . . . .	50
4.4.2	Penetration time . . . . .	50
4.4.3	Invasion pattern . . . . .	55
4.5	Conclusion . . . . .	56
<b>5</b>	<b>Pore-network Modeling of Dynamic Capillarity Effect during Fast Drainage</b>	
	<b>in Sandbox Experiments</b> . . . . .	<b>61</b>
5.1	Introduction . . . . .	63
5.1.1	Use of dynamic pore-network models for simulating experiments . . . . .	63
5.1.2	Dynamic capillary effect . . . . .	65
5.1.3	Aims and scopes . . . . .	66
5.2	Experimental setup and procedure . . . . .	66
5.3	Pore-network model description . . . . .	68
5.3.1	Model features . . . . .	68
5.4	Simulation results and discussion . . . . .	70
5.4.1	Computational domain, boundary and initial conditions . . . . .	70
5.4.2	Averaging of pore-network simulation data . . . . .	70
5.4.3	Quasi-static simulation of $P^c$ - $S^w$ curves . . . . .	71

5.4.4	Dynamic simulation . . . . .	72
5.5	Conclusion . . . . .	75
<b>6</b>	<b>Summary</b>	<b>77</b>
6.1	Benchmarking Volume-of-Fluid method . . . . .	77
6.2	Development of dynamic pore-network models and their applications	77
6.3	Recommendation . . . . .	79
<b>Appendix A Possible Fluid Distribution Patterns during Primary Imbibition</b>		<b>81</b>
<b>Appendix B Interfacial Area for A Cubic Pore Body</b>		<b>83</b>
B.1	Corner interfaces . . . . .	83
B.2	Main terminal menisci . . . . .	83
<b>References</b>		<b>85</b>



# Chapter 1

## Introduction

Complex geometry and flow events happening at different spatial and temporal scales make multiphase flow in porous media more difficult to model and simulate than its single phase counterpart, both at continuum scale and pore scale (Wooding and Morel-Seytoux, 1976). Continuum-scale modeling usually does not consider pore structure explicitly (Richards, 1931; Van Genuchten, 1980); pore geometry and topology can be used in direct pore-scale simulations, like Lattice Boltzmann (LB) method, Smoothed Particle Hydrodynamic (SPH) method, and Computational Fluid Dynamics (CFD) approaches or idealized in pore-network modeling (Blunt, 2001).

With the development of various visualization/imaging techniques (Kaestner et al., 2008) and micro-fluidics experiments, more pore-scale physics and higher spatial resolution can be obtained. These findings can help benchmarking and improving pore-scale models.

### 1.1 Benchmarking Volume-of-Fluid method

Given improvements in micromodel fabrication and experimental procedures, Ostrom et al. (2016) reported benchmarking pore-scale models against experimental data sets for non-reactive solute transport. All pore-scale models, including pore-network (PN) method, LB method and CFD technique, were able to satisfactorily reproduce the experiments. Although originally they planned to benchmark pore-scale models for multiphase flow, no paper on this topic has yet been published.

Horgue et al. (2013) used micromodels to study spreading of a liquid jet in a periodic array of cylinders. Experimentally they observed flow rate-dependent flow regimes. Their numerical simulation, using Volume of Fluid (VOF) method, qualitatively obtained

flow regimes similar to those observed in experiments. The main difference between simulation and experimental results concerned the precise values of the threshold flow rate for transitions from one regime to another.

Kunz et al. (2015) developed a SPH model and employed the model for simulation of experiments on two-phase flow in micromodels. Flow pattern was found to be in good agreement with experiment while process dynamics in experiment was not well reproduced; the invasion front was much slower in experiments.

Ferrari et al. (2015) presented comparison of VOF simulations and experiments for unstable primary drainage in porous micromodels. Same flux boundary condition was used in simulation as in experiment. No pressure was measured experimentally. Different invasion structure from experiment and numerical simulation was reported.

Xu et al. (2017) conducted simulations of drainage and imbibition experiments in a micromodel using LB method. Same viscosity ratio was used in simulation as in experiment while capillary number employed in simulation was 4 orders higher than experimental value. They found quantitatively good agreement in flow patterns between simulation and experiment.

Ling et al. (2017) investigated the reproducibility of pore-scale observations of multiphase flow experiments with small capillary number. Six replicates of the device were manufactured and up to five experiments were conducted in each replica. Small variability in flow patterns were observed in drainage experiments. They then used STAR-CCM+ (using finite volume discretization and VOF method for interface tracking) to simulate the experiments deterministically by imposing same flow rate as in experiment or stochastically by randomly varying flow rate. They demonstrated that these variations were due to sub-porescale geometry difference in microcells and variations in the boundary condition. No pressure information was mentioned.

This brief literature review shows that there still exists the need to validate and benchmark pore-scale multiphase flow models against experimental data. In this thesis, studies involving VOF method in OpenFOAM (Weller et al., 1998) for pore-scale simulations of multiphase flow in geometries of different complexities are presented. We focus on flow rate-pressure comparison between experimental observations and numerical simulations.

## 1.2 Pore-network modeling

With the development of imaging techniques and micro-fluidics experiments, pore-network models have evolved over decades to represent more complex structure and include more pore-scale physics (Blunt, 2001). Comprehensive reviews can be found in Joekar-Niasar and Hassanizadeh (2012b), Blunt et al. (2013) and Aghaei and Piri (2015).

Pore-network models can be categorized as quasi-static or dynamic. Quasi-static models have been successfully employed for prediction of relative permeabilities and capillary pressure-saturation relationship in multiphase system (Oren et al., 1998; Patzek, 2001; Piri and Blunt, 2005). A dynamic pore-network model is needed when capillary-dominance assumption is no longer valid and viscous force need to be considered together with capillary force. Dynamic pore-network models mainly fall into two groups: single-pressure algorithm and two-pressure algorithm.

Single-pressure algorithms are computationally efficient. However, they may suffer from several shortcomings: (1) network with regular geometry/topology; (2) failure to include corner flow/film flow; (3) ignorance of capillary pressure in pores; (4) rule-based description of interface morphology; (5) rule-based dynamic algorithm.

In two-pressure algorithm, both pore body and pore throat can be simultaneously occupied by both fluids, each having its own pressure. Interface position or shape in a pore is not explicitly described but included in pore body capillary pressure-saturation relationship. Pressure, flux and saturation are calculated separately for each fluid. This algorithm was initially developed by Thompson (2002) for study of imbibition process in fibrous materials. Later this algorithm was improved and implemented in a structured network with fixed coordination number of six to study theories of two-phase flow in porous media (Joekar-Niasar and Hassanizadeh, 2011a,b; Joekar-Niasar et al., 2010) and wicking behavior (Joekar-Niasar and Hassanizadeh, 2012a). In this work, we present our development of the two-pressure algorithm for unstructured network allowing for coordination number ranging from 1 to 26 (Raouf and Hassanizadeh, 2012). In this way, we can better mimic complex structures in real porous materials.

For two-phase flow involving two fluids with significantly different viscosities, like water-air system, pressure drop in the less viscous fluid may be negligible, and the above two-pressure algorithm may be simplified accordingly. We have developed a single-pressure algorithm for both drainage and imbibition.

Our models are employed to simulate liquid penetration into paper coating layer and to study dynamic capillarity effect during fast drainage in sandbox experiments.

### 1.3 Thesis outline

In Chapter 2, we present direct simulations of several experiments with different geometries using Volume of Fluid (VOF) method. Pressure-flow rate correspondence and flow patterns are compared between numerical and experimental data. For a simple geometry, we can reproduce experiments satisfactorily, while for complex geometries significant disagreement with experiment was observed. Possible reasons for these findings are analyzed.

In Chapter 3, we describe the development of pore-network models. A two-pressure dynamic drainage algorithm is developed for three-dimensional unstructured network model. Time step independence is discussed through drainage simulations. Dynamic effects in average phase pressure for fluid pairs with different viscosity ratios are studied using the code as an upscaling tool. Single-pressure algorithm for both drainage and imbibition are developed for cases where two fluids have significant viscosity difference, namely viscous pressure drop in one fluid may be negligible. Saturation pattern during imbibition for different boundary pressure drops are studied.

In Chapter 4, the single-pressure imbibition pore-network model is employed to simulate imbibition of wetting phase from a droplet into a paper coating layer. Geometry and topology of the pore network are based on FIB-SEM image of the coating material. Droplet sizes are chosen comparable with those of inkjet droplets. Penetration of different sizes of droplets with different material properties into pore network with different pore body and pore throat sizes are simulated.

In Chapter 5, the single-pressure pore-network model is employed study dynamic capillarity effect during drainage in a sandbox. The network is constructed based on sand grain size distribution, porosity, intrinsic permeability and quasi-static Pc-S curve from experimental measurements. Simulations show the ability of our model for dynamic simulations.

In Chapter 6, a summary of the research carried out here is presented and conclusions are discussed. Also, some recommendations are given.

## Chapter 2

# Direct Simulations of Two-phase Flow Experiments Using Volume-of-Fluid (VOF) Method

What is a model? A model is like an Austrian timetable. Austrian trains are always late. A Prussian visitor asks the Austrian conductor why they bother to print timetables. The conductor replies "If we did not, how would we know how late the trains are?"

---

*Victor Weiskopf*



## Abstract

We present direct simulations of several experiments with different geometries using Volume of Fluid (VOF) method. Pressure-flow rate correspondence and flow patterns are compared between numerical and experimental data. For a simple geometry, we can reproduce experimental results satisfactorily, while significant disagreement with experiment are observed for complex geometries. Possible reasons for these findings are analyzed. Direct pore-scale simulation of multiphase flow is promising, but further work on modeling and benchmarking with better controlled experiments is still needed.

### 2.1 Introduction

Complex geometry and flow events happening at different spatial, temporal scales make multiphase flow in porous media more difficult to model and simulate than its single phase counterpart, at both continuum-scale and pore-scale (Wooding and Morel-Seytoux, 1976). Continuum-scale modeling usually does not consider pore structure explicitly (Richards, 1931) (Van Genuchten, 1980) and in pore-scale network modeling (Blunt, 2001) we normally assume simplified geometry and topology. With the development of various visualization techniques (Kaestner et al., 2008), pore structure can be obtained with quite high spatial resolution. This high resolution geometry then can be used in direct numerical simulation methods, like Lattice Boltzmann (LB) method, Smoothed Particle Hydrodynamic (SPH) method and Computational Fluid Dynamics (CFD) approaches.

Given improvements in micromodel fabrication and experimental procedures, Oostrom et al. (2016) reported benchmarking pore-scale models against experimental data sets for non-reactive solute transport. All pore scale models, including pore network (PN) method, LB method and CFD technique, were able to satisfactorily reproduce the experiments. Although in this paper, they planned to benchmark pore-scale models for reactive transport and multiphase flow, no paper on this topic has yet been published.

## 8 | Direct Simulations of Two-phase Flow Experiments Using Volume-of-Fluid (VOF) Method

---

Horgue et al. (2013) used micromodels to study spreading of a liquid jet in periodic array of cylinders. Experimentally they observed flow rate dependent flow regimes. And their numerical simulation using Volume of Fluid (VOF) method qualitatively obtained flow regimes which are similar to those observed in experiments. The main difference between simulation and experiment concerned the precise values of the threshold flow rate for transitions from one regime to another. They proposed effects like dynamic films, complex menisci responsible for the discrepancy.

Kunz et al. (2015) developed a SPH model and applied the model for simulation of dynamic micromodel experiment. Flow pattern was found to be in good agreement with experiment while process dynamics in experiment was not well reproduced.

Ferrari et al. (2015) presented comparison of VOF simulations and experiments for unstable primary drainage in porous micromodels. Same flux boundary condition was used in simulation as in experiment. No pressure was measured experimentally. Different invasion structure from experiment and numerical simulation was reported. Three main sources of error were demonstrated: the uncertainty on the pore space geometry, the inaccuracy in initial condition and three-dimensional effects.

Xu et al. (2017) proposed a new algorithm for imposing contact angle in LB method. Further, simulation of drainage and imbibition experiments in pore-network micromodel were conducted. Same viscosity ratio was used in simulation as in experiment while capillary number employed in simulation was 4 orders higher than experimental value. They found quantitatively good agreement in flow patterns between simulation and experiment.

Ling et al. (2017) investigated the reproductivity of pore-scale multiphase flow experiments with small capillary number. Six replicates of the device were manufactured and up to five experiments were conducted in each replica. Smaller variability in flow patterns were observed in drainage experiments. They then used STAR-CCM+ (using finite volume discretization and VOF method for interface tracking) to simulate the experiment deterministically and stochastically by imposing same flow rate as in experiment or randomly varying flow rate. By this they demonstrated that these variations were due to sub-porescale geometry difference in microcells and variations in the boundary condition. No pressure information was mentioned.

Based on above literature review, there still exists the need to validate and further benchmark pore-scale multiphase flow models against experimental data. And we present the work involving VOF method in OpenFOAM (Weller et al., 1998) for pore scale simulation of multiphase flow in geometries of different complexities. We focus

on flow rate-pressure correspondence comparison between experiment and numerical simulation.

## 2.2 Numerical model description

### 2.2.1 Description of VOF method

For single phase flow we have classical Navier-Stokes equations giving mass and momentum balance (assume incompressibility and ignore external body forces):

$$\nabla \cdot \mathbf{u} = 0 \quad (2.1)$$

$$\frac{\partial \rho \mathbf{u}}{\partial t} + \nabla \cdot (\rho \mathbf{u} \mathbf{u}) = -\nabla p + \nabla \cdot (2\mu \mathbf{E}) \quad (2.2)$$

where  $\mathbf{u}$  is velocity,  $\rho$  is density and  $\mu$  is viscosity,  $\mathbf{E}$  is the deformation rate tensor,  $p$  is pressure.

For direct simulation of two-phase flow, we can solve Navier-Stokes equations in each phase and impose appropriate boundary conditions at the sharp fluid-fluid interface. But this generally requires interface fitting grids, which is impractical for cases involving interface merge or collapse. An alternative approach, VOF method has been introduced as diffuse interface model, in the sense that sharp interface is smoothed over layers of finite thickness. In this method, the computational domain is divided into 3 regions: two regions of each single phase and a transition layer region of interface. A volume fraction function,  $\alpha$ , is used to delineate the three regions:

$$\alpha = \begin{cases} 1 & \text{in the wetting phase} \\ 0 & \text{in the non-wetting phase} \\ (0, 1) & \text{interface region} \end{cases} \quad (2.3)$$

The interface force  $\mathbf{f}_s$  responsible for capillary pressure at interface is modeled as volume force, for smooth transition region with continuous  $\alpha$  (Brackbill et al., 1992)

$$\mathbf{f}_s \approx \mathbf{f}_v = \sigma k \nabla \alpha \quad (2.4)$$

## 10 | Direct Simulations of Two-phase Flow Experiments Using Volume-of-Fluid (VOF) Method

where  $\sigma$  is the interfacial tension between wetting phase and non-wetting phase,  $k$  is the curvature of interface and is defined as:

$$k = -\nabla \cdot \mathbf{n} = -\nabla \cdot \left( \frac{\nabla \alpha}{\|\nabla \alpha\|} \right) \quad (2.5)$$

$\mathbf{n}$  is the local normal unit vector.

To be consistent with mass and momentum balance equations in each single phase, density and viscosity are volume fraction function weighted:

$$\rho = \alpha \rho_w + (1 - \alpha) \rho_{nw} \quad (2.6)$$

$$\mu = \alpha \mu_w + (1 - \alpha) \mu_{nw} \quad (2.7)$$

Momentum balance equation evolves into:

$$\frac{\partial \rho \mathbf{u}}{\partial t} + \nabla \cdot (\rho \mathbf{u} \mathbf{u}) = -\nabla p + \nabla \cdot (2\mu \mathbf{E}) + \mathbf{f}_v \quad (2.8)$$

In each single phase region, Navier-Stokes equation still applies for that phase; while at interface domain where  $0 < \alpha < 1$ , extra volume force  $\mathbf{f}_v$  takes into account the capillary pressure drop across the interface. In OpenFOAM, to maintain sharpness of interface region, an artificial compression term is added to the transport equation of  $\alpha$ :

$$\frac{\partial \alpha}{\partial t} + \nabla \cdot (\alpha \mathbf{u}) + \nabla \cdot (\alpha(1 - \alpha) \mathbf{u}_r) = 0 \quad (2.9)$$

where compression velocity  $\mathbf{u}_r$  is formulated based on maximum velocity magnitude in the interface domain.

Contact angle  $\theta$  is included by condition at contact line:

$$\mathbf{n}_{\delta_s} = \mathbf{n}_s \cos \theta + \mathbf{t}_s \sin \theta \quad (2.10)$$

Where  $\mathbf{n}_s$  is the unit vector normal to the solid wall,  $\mathbf{n}_{\delta_s}$  is the unit vector normal to the interface and  $\mathbf{t}_s$  is the unit vector perpendicular to the contact line, tangent to and pointing into wetting-solid interface surface.

### 2.2.2 Corrected-two-dimensional model

Micromodel experiments are three-dimensional in nature, considering the relatively small and uniform depth, it is computationally efficient to solve the problem in two-dimension by taking into account effects from the depth direction (Horgue et al., 2013).

One effect is the viscous resistance from top and bottom substrates of the micromodel. Assuming trial velocity in the depth direction, Navier-Stokes equation can be integrated over the depth resulting an extra term:

$$\frac{\partial \rho \mathbf{u}}{\partial t} + \nabla \cdot (\rho \mathbf{u} \mathbf{u}) = -\nabla p + \nabla \cdot (2\mu \mathbf{E}) + \mathbf{f}_v - \frac{12\mu}{h^2} \mathbf{u} \quad (2.11)$$

where  $h$  is the depth of the micromodel.

The other effect is the interface shape change due to presence of top and bottom substrates. This effect can be geometrically approximated into extra curvature term for smooth  $\alpha$ :

$$k = -\nabla \cdot \left( \frac{\nabla \alpha}{\|\nabla \alpha\|} \right) - \frac{2}{h} \cos \theta \quad (2.12)$$

## 2.3 Experiments simulated in this study

In this study we employ VOF method to simulate two-phase flow in domains of three different geometry complexities.

### 2.3.1 Capillary rise experiment

This experiment was taken from Heshmati and Piri (2014), details can be found there. In the experiment a smooth glass tube of internal diameter 1 mm was vertically held with a Petri dish placed below it. To eliminate any curvature effects from edge of the dish, dish diameter was chosen as 9 cm. The glass tube was lowered slowly until it touched the water in the dish. The glass tube is water wet with zero static contact angle. Driven by capillary force, water will invade upwards into the tube. Water-air front was recorded during the process. Due to competition of capillary force, viscous force and gravity, imbibition front moves with decreasing speed and finally reaches at a steady position where capillary force balances with gravity.

**System parameters** Table 2.1 gives fluid properties used in the capillary rise simulation.

Table 2.1 Material properties for capillary rise experiment

Specification	Symbol	Value	Unit
Contact angle	$\theta$	0	degree
Interfacial tension	$\sigma^{wn}$	0.072	$kg s^{-2}$
Wetting fluid viscosity	$\mu^w$	0.001	$kg m^{-1} s^{-1}$

### 2.3.2 Micromodel experiments

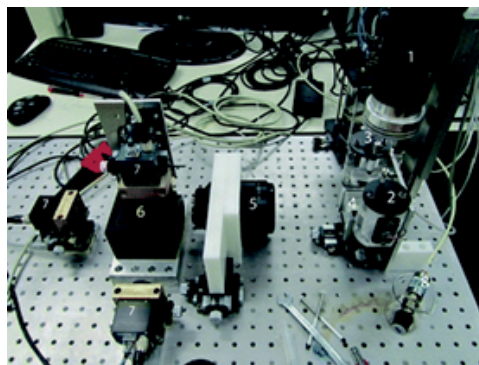


Fig. 2.1 Experimental setup

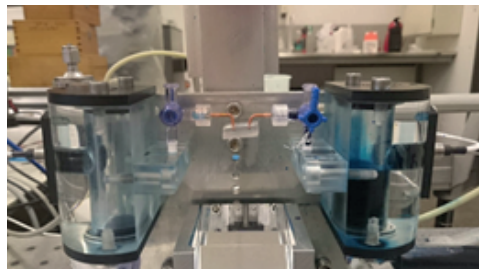


Fig. 2.2 Hydrodynamic part of the experiment system

The micromodel experimental setup is shown in Figure 2.1, details of the experimental system can be found at Karadimitriou et al. (2014). Two ends of the micromodel were connected with reservoirs where pump system controlled the pressure and pressure transducer measured the pressure, see hydrodynamic part of the experiment in Figure 2.2. The image acquisition system can record the fluid distribution in the micromodel over time. Information like saturation, interfacial area can be obtained from image analysis of the micromodels. Micromodel was fabricated of Poly-Di-Methyl-

Table 2.2 Material properties for micromodel experiments

Specification	Symbol	Value	Unit
Contact angle	$\theta$	40	degree
Interfacial tension	$\sigma^{wn}$	0.058	$kg s^{-2}$
Wetting fluid viscosity	$\mu^w$	0.047	$kg m^{-1} s^{-1}$
Non-wetting fluid viscosity	$\mu^n$	0.001	$kg m^{-1} s^{-1}$

Siloxane (PDMS). PDMS is hydrophobic, so flurinert was used as wetting phase and dyed water was used as non-wetting phase for better visualization. Table 2.2 gives fluid properties used in the micromodel experiments simulations. Drainage experiments were conducted. Initially the micromodel was filled with wetting phase flurinert with its inlet and outlet connected with non-wetting phase reservoir and wetting phase reservoir, respectively. Then, pressure in the non-wetting phase reservoir was increased and non-wetting phase invaded into micromodel as wetting phase receded into wetting phase reservoir.

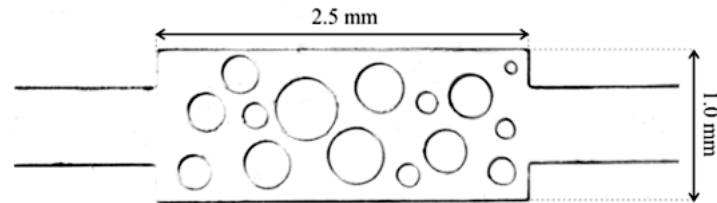


Fig. 2.3 Micromodel 1

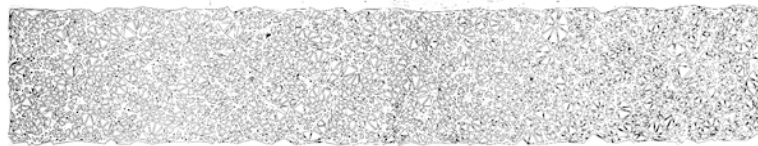


Fig. 2.4 Micromodel 2

Two micromodels of different geometries and topologies were used in the experiments: (1) The first micromodel (here after referred to as micromodel 1) is shown in Figure 2.3 with depth of  $100 \mu m$ . In the dynamic drainage experiment, pressure difference between inlet and outlet was set as 1860 Pa. (2) The second micromodel (here after referred to as micromodel 2) is shown in Figure 2.4 with depth of  $40 \mu m$ , the

size of the micro-model is about 5 mm by 30 mm. In the dynamic drainage experiment, pressure difference between inlet and outlet was set as 6300 Pa.

During the experiments boundary pressure drop across the micromodels were fixed and flow distribution in the micromodels were recorded over time. Information from measurement can be used in later numerical simulation comparison.

A single phase experiment in micromodel 1 was also performed using water as working fluid with fixed pressure drop of 1860 Pa. As there is no interface, steady state flow rate was obtained by collecting water at outlet for long enough time and this gives flow rate value as 0.319 mL/min.

## 2.4 Simulation results and discussion

### 2.4.1 Verification of corrected-two-dimensional model

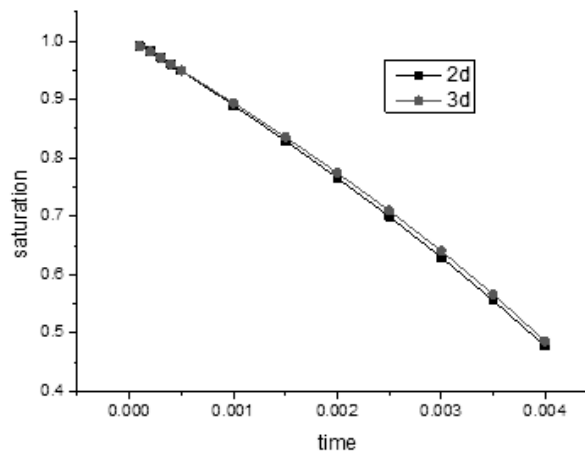


Fig. 2.5 Micromodel 2

To test whether the corrected 2D model can adequately account for effects of the third dimension, it was compared to the full 3-dimensional model. The comparison was done for drainage in a single duct with square cross section. The length of the conduct is 600  $\mu\text{m}$ , with cross section of 40 $\mu\text{m}$   $\times$  40 $\mu\text{m}$ . Saturation of flurinert during drainage with fixed pressure difference of 6000 Pa for 3D and corrected-2D simulation is shown in Figure 2.5. From this result, we can justify using corrected 2D model to

save computational time. Although for more complex geometries, bigger discrepancy may exist between 2D and 3D.

### 2.4.2 Capillary rise experiment

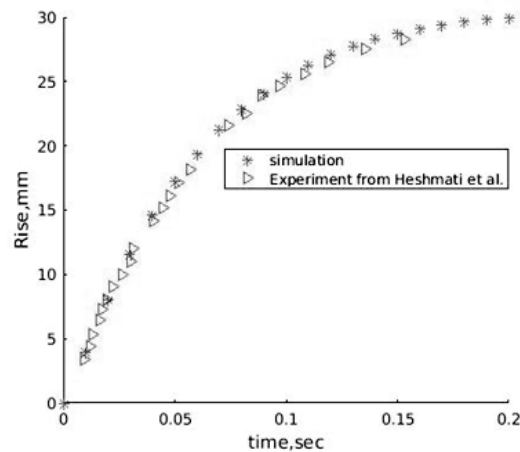


Fig. 2.6 Capillary rise comparison between experiment and simulation

Imbibition front position as function of time from simulation and experiment is compared in Figure 2.6. Constant zero static contact angle was used in simulation although original paper (Heshmati and Piri, 2014) investigated effects of dynamic contact angle. For this experiment of simple geometry, we observed good agreement between simulation and experimental data. This comparison shows fair validity of the VOF method in this case. This somehow corresponds to the fact that Washburn equation has been tested valid for capillary radius down to  $3 \mu\text{m}$  (Zhmud et al., 2000). One issue to mention: here computational domain should include part of the dish where we impose hydrostatic pressure boundary condition and simulation with only capillary tube will result in faster invasion than experiment.

### 2.4.3 Micromodel experiments

Same fixed pressure drop boundary conditions were imposed in simulations as in experiments. We are interested mainly in two aspects: how is the flow pattern agreement between simulation and experiment and can we capture the dynamics of the invasion process?

**Experiment in micromodel 1** For single phase water experiment with same fixed boundary pressure as in experiment, simulation gave steady flow rate of 0.594mL/min, 1.86 times of experiment measurement of 0.319mL/min.

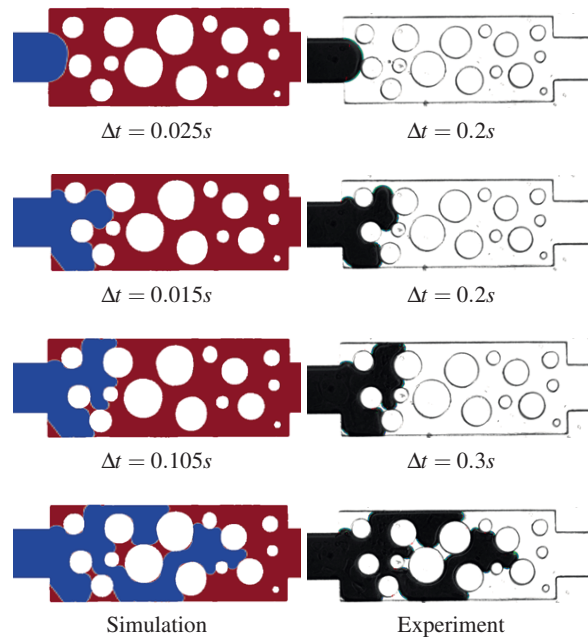


Fig. 2.7 Comparison between simulation and experiment for micromodel 1

Comparison between simulation and experiment is shown in Figure 2.7 , where similar flow pattern is chosen between simulation and experiment, also time intervals between two snapshots are given. Experimental flow patterns are well reproduced. In terms of kinetics we cannot reproduce experimental results satisfactorily. There are more energy dissipations in experiments.

**Primary drainage experiment in micromodel 2** As shown in Figure 2.8, there is more disagreement between experimental data and simulation in terms of both dynamics and flow pattern. Invasion happened much slower in experiment than in simulation, which means that more resistance exists in experiments, the same as in micromodel 1. However, flow pattern was poorly predicted against experiment.

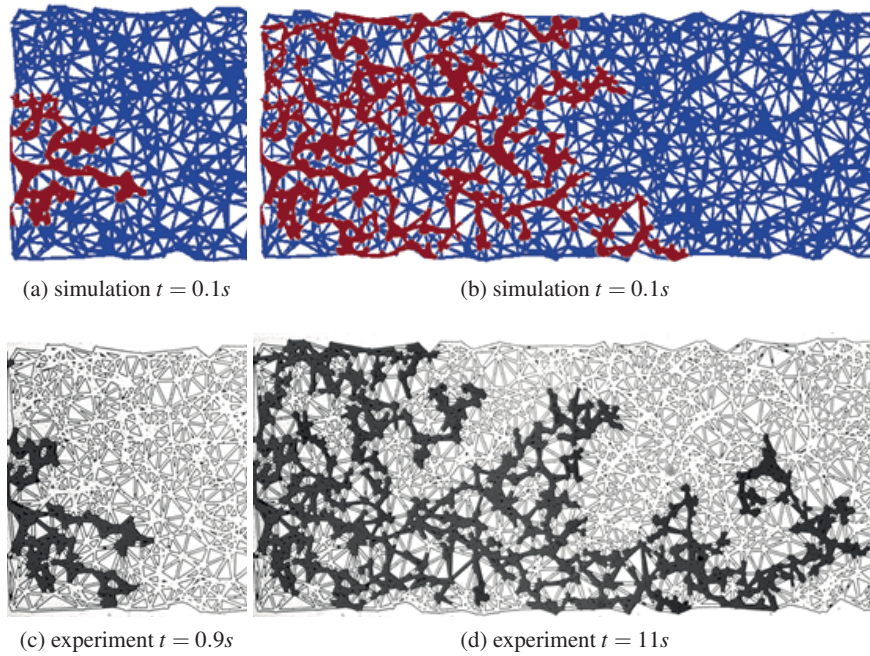


Fig. 2.8 Comparison between simulation and experiment for micromodel 2

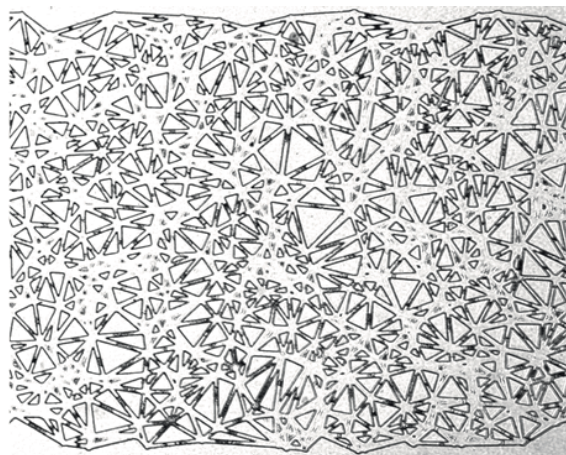


Fig. 2.9 Part of micromodel 2 showing roughness

#### 2.4.4 Discussions

Our simulations show good agreement between numerical simulations and experimental data for capillary rise experiment and discrepancy for micromodel experiments.

For single phase flow, Navier-Stokes equations are pretty mature and established models. For micromodel 1, disagreement between simulation and experiment measurement may be attributed to possible pressure loss at connection between computational domain and pressure measurement points. Invisible roughness on the wall may also introduce excess dissipation.

For capillary rise experiment, the smooth glass tube, the regular geometry and the well correspondence of initial condition and boundary condition between simulation and experiment may help for satisfactorily reproducing the experimental measurement.

For two-phase flow in micromodel experiments, arguments for single phase flow simulation in micromodel 1 still apply. Other effects, like interface modeling, “pinning” of contact line and 3D effects, may introduce extra errors.

In VOF method, interface is not explicitly tracked and there exists a interface with several cells thickness. Volume fraction in this finite thickness layer is used to calculate the interface normal and curvature for the interface region, which could be inaccurate. Deshpande et al. (2012) reported 10% error in interface curvature computation by VOF method from analytical value. Also interfacial tension is modelled as a body force, at discrete level, we may have force imbalance between interfacial tension and other body forces. These two effects give rise to the so called “parasitic currents” (Wörner, 2012). These effects may partly explain discrepancy in our simulations of two-phase flow in micromodel 1 and 2.

There may exist many invisible roughness inside micromodel 1 and 2 due to fabrication. “Pinning” of contact line can also play a role. A threshold stress value may exist below which there is no displacement of contact line. Excess force may be needed to move the contact line and keep it moving, especially for rough surface. These effects may not only give contact angle hysteresis but also introduce extra viscous losses near vicinity of interface and especially near the contact line where fluid may experience very high stress (Dullien, 1992). In our drainage experiment higher capillary pressure due to pinning will slower the process, this agrees well with the faster invasion in simulation than experiment. So it is rather probable that for same fixed pressure drop, in experiment more energy was consumed at the interface and contact line region than in numerical simulation. So numerical model produced faster invasion and this may accumulate over time to give us the discrepancy in Figure 2.7 and Figure 2.8.

To save computational time, we have used 2D model. Although we find good agreement between 2D and 3D model in Figure 2.5. Disagreement will emerge for irregular geometry in micromodel 1 and 2, as we assume zero flux in depth direction. The 3D effects of roughness inside the micromodel can give rise more errors.

In terms of flow pattern, for micromodel 1, good numerical results are probably due to stronger capillary effects than viscous effects and relatively simple geometry. For failure of flow pattern prediction of micromodel 2 in Figure 2.8, this may be largely due to the small “islands”/roughness in the micromodel from fabrication process as shown in Figure 2.9. On one hand, sizes of these “islands”/roughness are unknown, on the other hand, meshing along these “islands”/roughness would be an issue. So these “islands”/roughness were not included in our computational domain, and they may induce more viscous resistance and higher capillary barrier and thus also influence the flow pattern. Moreover, due to the more complex geometry of this micromodel, initial small discrepancy between experiment and simulation may be amplified and lead to different flow pathways.

## 2.5 Summary and Conclusion

In this paper, we employed VOF method to simulate two-phase flow experiments of different geometries. For simple geometry and smooth solid surface, like single capillary rise experiment, VOF simulation gave good agreement between simulation and experiment. But for micromodels with complex geometry and possible rough surface, we may be able to predict the flow pattern while cannot capture the dynamics of the process like for micromodel 1. Or we failed in both flow pattern and dynamics prediction as in micromodel 2. Reasons for failure in reproducing experimental data are discussed.

With the development of visualization techniques, more detailed pore-scale geometry can be obtained. Still we should be careful with employing this geometry in direct pore-scale simulation of multiphase flow.

Direct pore-scale simulation of multiphase flow itself and its help in upscaling are promising. But more work regarding modeling and benchmarking with better controlled experiments is still needed.



## Chapter 3

# Dynamic Pore-network Models Development

Tell a man there are 300 billion stars  
in the universe and he'll believe you.  
Tell him a bench has wet paint on it  
and he'll have to touch to be sure.

---

*Anonymous*



## Abstract

A two-pressure dynamic drainage algorithm is developed for three-dimensional unstructured network model. The impact of time step is discussed through drainage simulations. Dynamic effects in average phase pressure for fluid phases with different viscosity ratios are explored using the developed code as an upscaling tool. For cases where two fluids have significant viscosity differences, the viscous pressure drop within one fluid may be neglected. This dynamic algorithm can be further simplified into a single-pressure algorithm. This simplifications have been done for both drainage and imbibition. Saturation pattern during imbibition for different boundary pressure drops are studied. With increase of boundary pressure, invasion becomes less capillary dominant with a wetting front.

### 3.1 Introduction

Along with the development of imaging techniques and micro-fluidics experiments, pore-network model has evolved over decades to represent more efficient and complex structures with more pore-scale mechanisms included.

Pore-network can be categorized as quasi-static or dynamic. Quasi-static models have been successfully applied for the prediction of relative permeabilities, capillary pressure-saturation in multiphase system (Oren et al., 1998; Patzek, 2001; Piri and Blunt, 2005). Dynamic pore-network model applies when capillary-dominance assumption is no longer valid and viscous forces need to be considered together with the capillary forces. Dynamic pore-network models mainly fall into two groups: single-pressure algorithm and two-pressure algorithm. We discussed several representative already developed pore network models below and comprehensive reviews can be found in Joekar-Niasar and Hassanizadeh (2012b), Blunt et al. (2013) and Aghaei and Piri (2015).

Blunt and King (1990) simulated two-phase flow using isotropic pore network to study invasion fractal dimension and dynamic relative permeability. In their model,

throats were completely filled with only fluid while pores may contain two fluids simultaneously. Capillary pressure in pores were neglected.

van der Marck et al. (1997) studied drainage by means of experiments and simulation methods. They extended the numerical pore-network model by Lenormand et al. (1988). They compared pressure buildup at boundary and saturation in the domain before breakthrough during flow controlled drainage process. Pressure is defined at pores and pores could be occupied by two fluid. Only capillary pressure at channels were considered and capillary pressure at pores were neglected. The algorithm mainly involved pressure solving and saturation update.

Aker et al. (1998) modeled the dynamics of drainage dominated flow using a two-dimensional network. The flow front width from simulation was found to be consistent with a scaling relation and scaling exponents were compared with experimental data from the literature. Pressure was defined at nodes and only one fluid would occupy a node. Main terminal meniscus is modeled while film flow and corner flow were not considered. Simultaneous flow of two liquids into one tube was allowed with maximum two menisci. Solving volume flux conservation at nodes provided pressure field. Rules were defined to describe how a meniscus will move into neighboring tubes when it reaches the end of a tube.

Al-Gharbi and Blunt (2005) presented a dynamic network model for modeling of two-phase drainage. Wetting layer flow, meniscus oscillation, and the dynamics of snap-off are accounted for. In their model, pressure are assigned at pore centers and throat centers. Volume conservation equations for pores and throats determines pressure field. In writing pressure drop between neighboring pore and throat, number and orientation of interface are included. After solving pressure, location of interface can be updated by iteration. Rules regarding invasion of pore center and fusion of interface are defined to ensure relatively simple track of number and orientation of interface.

These single-pressure algorithms may be computationally efficient, however, they could suffer from: (1) network with regular geometry/topology; (2) failure to include corner flow/film flow; (3) ignorance of capillary pressure at pores; (4) rule-based description of interface morphology; and (5) rule-based dynamic algorithm.

Using a two-pressure algorithm, both pore body and pore throat can be filled with different fluids, each with its own pressure. Interface position or shape is not explicitly described but included in pore body capillary pressure-saturation relationship. Pressure, fluxes and saturations are calculated separately for each fluid. This algorithm was ini-

tially developed by Thompson (2002) for study of imbibition process in fibrous materials. Later this algorithm was improved and implemented onto structured network with fixed coordination number of six to study theories of two-phase flow in porous media (Joekar-Niasar and Hassanizadeh, 2011a,b; Joekar-Niasar et al., 2010) and wicking behavior (Joekar-Niasar and Hassanizadeh, 2012a).

In this work we present development of the two-pressure algorithm for unstructured network allowing for coordination number ranging from 1 to 26 introduced by Raouf and Hassanizadeh (2012). For two-phase flow involving two fluids with significant different viscosities, such as the water-air system, pressure drop in less viscous fluid may be negligible, and the above two-pressure algorithm may be simplified accordingly. Single-pressure algorithms for both drainage and imbibition are developed in this study.

We give description of our algorithms in Section 3.2 and simulations are carried out in Section 3.3.

## 3.2 Pore-network model description

### 3.2.1 Model features

**Structure and geometry** Pore bodies are cubic and pore throats have square cross sections. With these shapes of pore bodies and pore throats, we need to have inscribed radii of pore throats, inscribed radii of pore bodies, length of pore throats and coordination number. We can either generate the unstructured network based on some distributions, such as log-normal distribution, and tune geometrical and topological data to match the available experimental measurements when necessary; Or we can model random geometry and topology directly using information from network extraction methods, like Avizo (FEI Visualization Sciences Group). Our algorithms can handle these two kinds of networks. Here we will generate the unstructured network described in Raouf and Hassanizadeh (2012). Figure 3.1 provides the distribution of inscribed radii sizes of pore throats, inscribed radii sizes of pore bodies, length sizes of pore throats and coordination number.

**Assumptions** Assumptions employed in the pore-network algorithm are as follows:

1. The volume of pore throats are assumed to be negligible compared to the volume of pore bodies. This means that the filling of a pore throat is assumed to occur in no time.

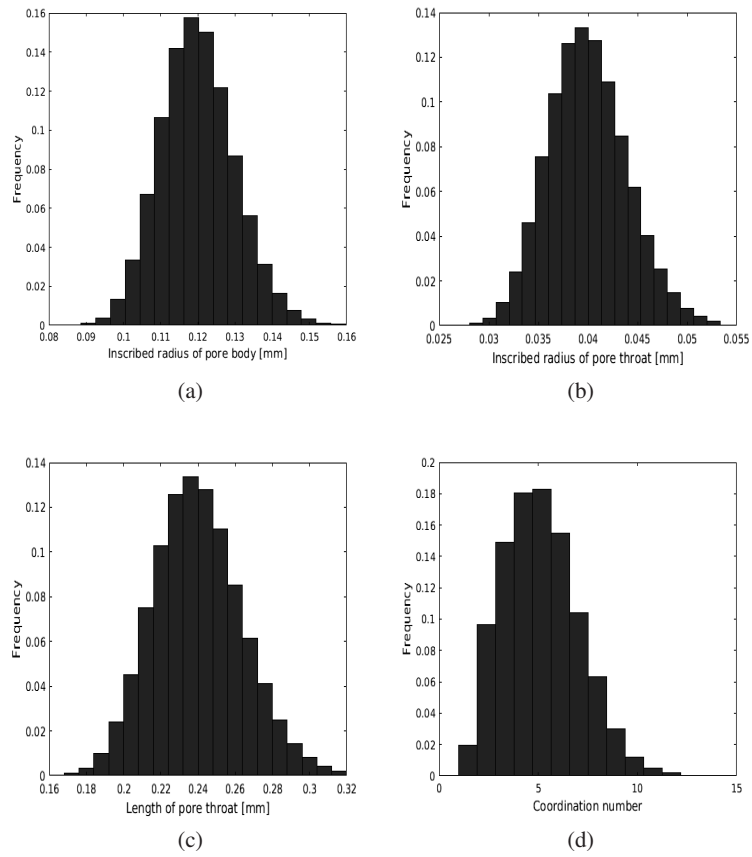


Fig. 3.1 Size distribution of (a) inscribed radii of pore throats; (b) pore throats length; (c) inscribed radii of pore bodies; (d) coordination number

Table 3.1 Material properties

Specification	Symbol	Value	Unit
Contact angle	$\theta$	0	degree
Interfacial tension	$\sigma^{wn}$	0.072	$kg s^{-2}$
Wetting fluid viscosity	$\mu^w$	0.001	$kg m^{-1} s^{-1}$
Non-wetting fluid viscosity	$\mu^n$	0.01 or 0.001 or 0.0001	$kg m^{-1} s^{-1}$

2. No hydraulic resistance is assigned to pore bodies; their resistance to the flow is assumed to be negligible compared to that of pore throats.
3. No gravity effects is included.
4. Flow of wetting phase through corners of pore elements is taken into account. Therefore, any pore body or pore throat can be simultaneously occupied by both wetting phase and non-wetting phase.

**System parameters** Table 3.1 gives fluid properties used in the simulations. Three values of non-wetting phase viscosities are adopted to have 3 viscosity ratios of  $M(= \frac{\mu^n}{\mu^w})$ : 10, 1, 0.1.

### 3.2.2 local rules

**Capillary pressure for pore bodies** Assuming that the wetting phase resides symmetrically in all eight corners of pore bodies, capillary pressure-saturation relationship for cubic pore bodies can be as (Joekar-Niasar et al., 2010):

$$p_i^c(s_i^w) = p_i^n - p_i^w = \frac{2\sigma^{wn} \cos\theta}{R_i(1 - \exp(-6.83s_i^w))} \quad (3.1)$$

where  $p_i^c$  is capillary pressure,  $p_i^\alpha$  and  $s_i^\alpha$  denote pressure and saturation of  $\alpha$  phase in pore body  $i$ , and  $R_i$  is the radius of inscribed sphere of pore body  $i$ . Here, we have not considered the possibility for different interface shapes in a pore body due to different filling states of its neighbors (Lenormand et al., 1988).

**Entry capillary pressure for pore throats** Entry capillary pressure for a square pore throat is defined as (Mason and Morrow, 1991; Mayer and Stowe, 1965; Princen, 1970):

$$p_{ij}^{en} = \frac{\sigma^{wn}}{r_{ij}} \left( \frac{\theta + \cos^2 \theta - \pi/4 - \sin \theta \cos \theta}{\cos \theta - \sqrt{\pi/4 - \theta + \sin \theta \cos \theta}} \right) \quad (3.2)$$

where  $r_{ij}$  is the radius of inscribed circle of pore throat cross section.

**Minimum wetting phase saturation in a pore body** Due to existence of corners, during drainage wetting phase will not be completely displaced from pore bodies. The minimum wetting phase saturation of each pore body is defined according to the global pressure difference, namely:

$$P_{global}^c = P_{inlet}^n - P_{outlet}^w \quad (3.3)$$

$$s_{i,min}^w = -\frac{1}{6.83} \ln \left( 1 - \frac{1}{R_i} \frac{2\sigma^{wn} \cos \theta}{P_{global}^c} \right) \quad (3.4)$$

### Invasion criteria and trapping

**A. Drainage** When non-wetting phase pressure in a pore body exceeds the entry capillary pressure of its neighboring pore throats, non-wetting phase will invade the pore throat.

**B. Single-phase imbibition** From one time step to another, a pore throat will be assumed to get invaded by the wetting phase only if at least one of its neighboring pore bodies has reached a wetting phase saturation of 0.477 (corresponding to the case where the non-wetting phase filling the inscribed sphere of the pore body). At first, only corners are assumed to become filled. The radius of the meniscus formed in the corner depends on the wetting phase pressure, and is given by Equation.(3.9) below.

If the wetting phase pressure in one of the neighboring pore bodies is high enough, the whole pore cross section will be invaded by the wetting phase. So the criteria for the full invasion of a pore throat is  $p_{ij}^c < p_{ij}^{en}$  by wetting phase in unsaturated neighboring pore body. For wetting phase saturated pore body, wetting phase will invade the narrower pore throat through main terminal meniscus. However, even if one or both invasion criteria, which were just described, are met, a pore throat will not be

invaded if it is considered to be trapped (Al-Futaisi and Patzek, 2003). Details about different scenarios of invasion and trapping can be found in appendix A.

In general, when a pore throat is not considered to be trapped, it can always be invaded by the wetting phase (independent of the applied boundary pressure) since corner flow can always occur. However, we have imposed the requirement that the saturation of one of the neighboring pore bodies must exceed 0.477.

**Conductivities of pore throats** The conductivities of phases through pore throats depend on fluids occupancy in the pore throat cross section. In general, we may have the following states:

1. Pore throat is fully occupied by wetting phase. Its conductivity is given by (Azzam and Dullien, 1977).

$$K_{ij}^w = \frac{\pi}{8\mu^w l_{ij}} r_{ij}^{eff4} \quad (3.5)$$

where  $l_{ij}$  is length of pore throat and

$$r_{ij}^{eff} = \sqrt{\frac{\pi}{4}} r_{ij} \quad (3.6)$$

2. Pore throat is occupied by wetting phase in the corner while non-wetting phase is in the middle (Ransohoff and Radke, 1988).

$$K_{ij}^w = \frac{4 - \pi}{\beta \mu^w l_{ij}} r_{ij}^c{}^4 \quad (3.7)$$

$$K_{ij}^n = \frac{\pi}{8\mu^n l_{ij}} r_{ij}^{eff4} \quad (3.8)$$

where

$$r_{ij}^c = \frac{\sigma^{wn}}{p_{ij}^c} \left( \frac{\theta + \cos^2 \theta - \pi/4 - \sin \theta \cos \theta}{\cos \theta - \sqrt{\pi/4 - \theta + \sin \theta \cos \theta}} \right) \quad (3.9)$$

$$r_{ij}^{eff} = \frac{1}{2} \left( \sqrt{\frac{r_{ij}^c{}^2 - (4 - \pi)r_{ij}^c{}^2}{\pi}} + r_{ij} \right) \quad (3.10)$$

Dimensionless resistance  $\beta$  is given by Zhou et al. (1997). For single-pressure algorithm, only wetting phase conductivity will be used.

**Snap-off** Snap-off may happen in a pore throat when capillary pressure in the pore throat drops below a threshold value so that stable corner interface is not supported any more. For square cross-sectioned pore throat, ignoring dynamic contact angle effects, the criterion on snap-off is defined as (Vidales et al., 1998):

$$p_{ij}^c \leq \frac{\sigma^{wn}}{r_{ij}} (\cos\theta - \sin\theta) \quad (3.11)$$

Once snap-off happens in a pore throat, it will be fully occupied by the wetting phase and its conductivity will be changed accordingly.

### 3.2.3 Governing equations

**Governing equations and saturation update for two-pressure drainage** For two-pressure algorithm, fluid volume balance equation in pore bodies can be written resulting in linear system of equations:

$$\sum_{j=1}^{N_i} [(K_{ij}^w + K_{ij}^n)p_i^w - (K_{ij}^w + K_{ij}^n)p_j^w] = - \sum_{j=1}^{N_i} K_{ij}^n (p_i^c - p_j^c) \quad (3.12)$$

where  $N_i$  is coordination number of pore body  $i$ .

After solving pressure field, saturation can be updated explicitly:

$$V_i \frac{\Delta s_i^w}{\Delta t} = -q_i^w = - \sum_{j=1}^{N_i} K_{ij}^w (p_i^w - p_j^w) \quad (3.13)$$

where  $V_i$  is volume of pore body  $i$ ,  $\Delta t$  is time step,  $q_i^w$  is total wetting phase flux of pore body  $i$ .

**Governing equations for single-pressure imbibition** A single-pressure primary imbibition algorithm is developed for the case where a viscous fluid is the wetting phase and a much less viscous fluid (like air) is the non-wetting phase. Wetting phase pressure will be calculated while the non-wetting phase is assumed to be at a constant and uniform pressure at all times. This is a valid assumption given the negligible viscosity of the non-wetting phase.

Local ( i.e., the pore level) capillary pressure for a given pore body  $i$  is defined in Section 3.2.2. Initially, all pore bodies are assumed to have a initial wetting phase saturation (we set  $s_{init}^w = 0.5\%$ ) except the inlet pore bodies which remain saturated at all times. Those boundary pore bodies are assumed to be fully saturated. Thus, initially

all internal pore bodies have a large negative wetting phase pressure given by  $p_i^c(s_i^w)$  relationship (we have imposed a maximum of  $p_i^c$  of  $10^6$  Pa ). Saturated boundary pores are assigned the same pressure as inlet reservoir.

Infiltration starts by the wetting phase flowing from the saturated boundary pores into the internal pores. Their saturation, and thus their pressure rise and, subsequently, wetting phase can flow into the neighboring pores. The wetting phase flow occurs via pore throats and its rate can be calculated using Hagen-Poiseuille formula:

$$Q_{ij}^w = K_{ij}^w(p_i^w - p_j^w) \quad (3.14)$$

The saturation update for each pore body is made based on volume balance equation, the same as in Equation (3.13). The calculation is done fully explicitly. Note that the saturation update needs to be done for active unsaturated pore bodies, those for which at least one pore throat has been invaded by wetting phase. As long as no internal pore body has become fully saturated with wetting phase, the updating of pore body saturation and pressure, invasion of new pore throats and the next cycle of flow calculation, and the updating of saturation and pressure continues. However, at each step, we check whether a given pore throat can be invaded by the wetting phase, following the criteria discussed in Section 3.2.2.

As soon as one or more internal pore bodies become fully saturated with the wetting phase, then we have to solve for the pressure of those pore bodies based on the following volume balance equation:

$$\sum_{j=1}^{N_i} K_{ij}^w(p_i^w - p_j^w) = 0 \quad (3.15)$$

Here,  $K_{ij}^w$  is calculated explicitly. The domain of saturated pore bodies is surrounded by unsaturated pore bodies. The pressure of unsaturated pore bodies (known from the current time step) is used as boundary condition values for the domain of saturated pore bodies. Once the pressure of all saturated pore bodies are calculated, steps described above for updating saturation of unsaturated pore bodies will be repeated.

Figure 3.2 gives schematic diagram of the domain with boundary pores and internal saturated and unsaturated pores, where blue color shows the wetting phase and red color shows the non-wetting phase. In this figure, pore bodies are denoted from A to I and pore throats are denoted from 1 to 12. A, B, C are boundary pore bodies, E is internal saturated pore body, D, F, H are internal unsaturated pore bodies and G, I are pore bodies that are not invaded yet. Depending on invasion criteria, pore throats {3,4,5,6,7,9} are invaded and fully occupied by the wetting phase while pore throats

{8,10,11,12} are not invaded yet. No initial tiny saturation is shown in the figure and no attempt is made to represent the real interface shape.

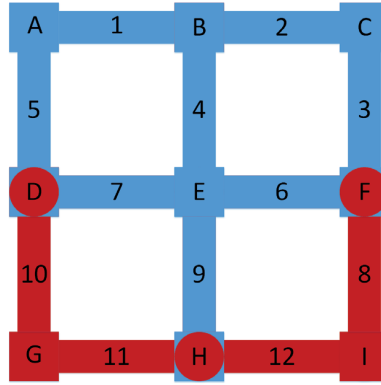


Fig. 3.2 Schematic diagram of boundary pores, internal unsaturated pores and saturated pores in single-pressure imbibition algorithm

**Governing equations and saturation update for single-pressure drainage** In this single-pressure algorithm, the volume balance equation for the wetting phase of a pore body results in the following system of equations:

$$V_i \frac{\Delta s_i^w}{\Delta t} = -q_i^w \quad (3.16)$$

where  $q_i^w$  is total wetting phase flux of pore body  $i$ ,  $V_i$  is volume of pore body  $i$ ,  $\Delta t$  is time step. For wetting saturated pore bodies that are not invaded by non-wetting phase,  $q_i^w = 0$ .

Based on Eq.(??) and as we assume air pressure to be constant, using chain rule of differentiation, we can rewrite Eq.(3.16) as:

$$V_i \frac{ds_i^w}{dp_i^w} \frac{\Delta p_i^w}{\Delta t} = - \sum_{j=1}^{N_i} Q_{ij}^w \quad (3.17)$$

where  $N_i$  is coordination number of pore body  $i$ ,  $Q_{ij}^w$  is wetting phase flux in pore throat  $ij$  given by Hagen-Poiseuille formula and  $\frac{ds_i^w}{dp_i^w} = -\frac{ds_i^w}{dp_i^w}$  (this also holds for  $s_i^w = 1$ ). Thus, Eq.(3.17) may be written in discretized form as:

$$V_i \frac{ds_i^w}{dp_i^w} \frac{(p_i^w)^{k+1} - (p_i^w)^k}{\Delta t} = - \sum_{j=1}^{N_i} K_{ij}^w ((p_i^w)^{k+1} - (p_j^w)^{k+1}) \quad (3.18)$$

Rearranging terms, we obtain the following equation, which should be solved for obtaining  $p_j^w$  at new time level  $k + 1$ .

$$\left( \frac{V_i}{\Delta t} \frac{ds_i^w}{dp_i^w} + \sum_{j=1}^{N_i} K_{ij}^w \right) (p_i^w)^{k+1} - \sum_{j=1}^{N_i} K_{ij}^w (p_j^w)^{k+1} = \frac{V_i}{\Delta t} \frac{ds_i^w}{dp_i^w} (p_i^w)^k \quad (3.19)$$

To emphasize solving pressure  $p_j^w$  for new time level  $k + 1$ , only time level ( $k$  or  $k + 1$ ) for pressure is given by superscript and  $K_{ij}^w$ ,  $\frac{ds_i^w}{dp_i^w}$  are evaluated at time level  $k$ .

If gravity is considered as in Chapter 5:

$$\left( \frac{V_i}{\Delta t} \frac{ds_i^w}{dp_i^w} + \sum_{j=1}^{N_i} K_{ij}^w \right) (p_i^w)^{k+1} - \sum_{j=1}^{N_i} K_{ij}^w (p_j^w)^{k+1} = \frac{V_i}{\Delta t} \frac{ds_i^w}{dp_i^w} (p_i^w)^k - \sum_{j=1}^{N_i} K_{ij}^w \rho^w g (z_i - z_j) \quad (3.20)$$

where  $z_i$  is position of pore body  $i$  in  $z$ -direction.

After solving pressure field, wetting phase flux of pore bodies can be calculated and saturation of pore bodies will be updated the same as in Equation (3.13).

Similarly, if gravity is considered, saturation is updated based on:

$$V_i \frac{(s_i^w)^{k+1} - (s_i^w)^k}{\Delta t} = - \sum_{j=1}^{N_i} K_{ij}^w ((p_i^w)^{k+1} - (p_j^w)^{k+1} + \rho^w g z_i - \rho^w g z_j) \quad (3.21)$$

### 3.2.4 Time step

**Imbibition** During imbibition, time step  $\Delta t$  is taken to be equal to the smallest filling time  $\Delta t_i$  of all active unsaturated pore bodies, but it is possible to have local drainage in some pore bodies. Allowing pore bodies to be infiltrated to  $s_i^w = 1$  or drained to  $s_i^w = 0$ .  $\Delta t_i$  is determined as:

$$\Delta t_i = \begin{cases} \frac{V_i}{q_i^w} (s_i^w) & q_i^w > 0 \\ \frac{V_i}{q_i^w} (1 - s_i^w) & q_i^w < 0 \end{cases} \quad (3.22)$$

A global time step is then selected as the minimum time step of all pore bodies:

$$\Delta t = \min\{\Delta t_i\} \quad (3.23)$$

A saturation truncation value of  $10^{-3}$  is adopted to ensure finite time step. When local saturation in a pore body is close to the target saturation values within the truncation value, that pore body will not be included in global time step determination.

**Drainage** Time step is determined based on filling or emptying of pore-bodies:

$$\Delta t_i = \begin{cases} \frac{V_i}{q_i^w} (s_i^w - s_{i,\min}^w) & q_i^w > 0 \\ \frac{V_i}{q_i^w} (1 - s_i^w) & q_i^w < 0 \end{cases} \quad (3.24)$$

The global time step is selected as the minimum time step of all pore bodies:

$$\Delta t = C_{oe} \min(\Delta t_i) \quad (3.25)$$

A same saturation truncation of  $10^{-3}$  is adopted to ensure finite time step. A time-step coefficient  $C_{oe}$  smaller than 1 is adopted. Discussion on this coefficient can be found in Section 3.3

### 3.2.5 Computational procedure

**Single-phase imbibition** The procedure for dynamic primary imbibition simulation is:

1. Set boundary condition and initial condition for the pore network;
2. Determine conductivity of pore throats based on fluid occupancy as well as trapping and invasion criteria;
3. Solve wetting phase volume balance equations for the saturated pore bodies and get pressure field;
4. Calculate flux based on conductivity determined in step 2, determine time step;
5. Update saturation and pressure of unsaturated active pore bodies;
6. Go to Step 2 and repeat the process.

**Drainage** The procedure for dynamic drainage simulation is:

1. Set boundary condition and initial condition for the pore network;
2. Determine conductivity of pore throats based on invasion criteria;
3. Solve mass balance equations to get the pressure field;
4. Calculate flux, determine time step and update saturation of pore bodies;
5. Go to step 2 and repeat the process.

### 3.3 Simulations and discussions

#### 3.3.1 Boundary conditions

For 3D network, we assume the network is connected with a wetting reservoir at one end and with a non-wetting phase reservoir at the other end. During drainage, the face connected with the non-wetting phase reservoir is considered as inlet and the other face is considered as the outlet; during imbibition, the place of inlet and outlet are exchanged.

#### 3.3.2 Averaging procedure

Pore-network simulations provide pore-scale information including pressure and saturation. To upscale these quantities to the macroscopic quantities, we need to define averaging operators for these variables.

$$S^\alpha = \frac{\sum_{i=1}^{N_b} s_i^\alpha V_i}{\sum_{i=1}^{N_b} V_i}, \alpha = n, w \quad (3.26)$$

$$P^\alpha = \frac{\sum_{i=1}^{N_b} p_i^\alpha s_i^\alpha V_i}{\sum_{i=1}^{N_b} s_i^\alpha V_i}, \alpha = n, w \quad (3.27)$$

$$P^c = \frac{\sum_{i=1}^{N_b} p_i^c A_i^{wn}}{\sum_{i=1}^{N_b} A_i^{wn}} \quad (3.28)$$

Here pore-scale pressure is averaged over volume to obtain the macroscopic pressure and capillary pressure is averaged over interfacial area to provide the macroscopic capillary pressure. Interfacial area in cubic pore bodies are given in Appendix B.

#### 3.3.3 Two-pressure drainage simulations

**REV size** Figure 3.3 shows quasi-static drainage simulations for different network sizes with the same statistical parameters provided in Figure 3.1. It is clear that a network size of 25 can be considered as REV (Representative Elementary Volume).

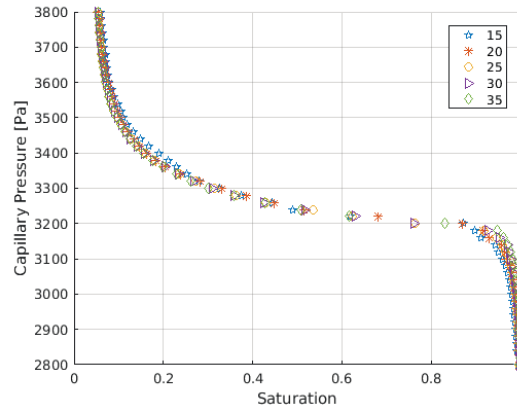


Fig. 3.3 Quasi-static  $P^c - S^w$  curves for different network sizes

**Time step independence** In dynamic pore network models, time step is usually determined based on filling/emptying of pore bodies, in a manner that no more than one pore body is filled or emptied during one time step. A minimum time step value may also be imposed to save computational time. However, the effect of time step value is discussed. We check the impact of time step by altering coefficient  $C_{oe}$  in Equation (3.25).

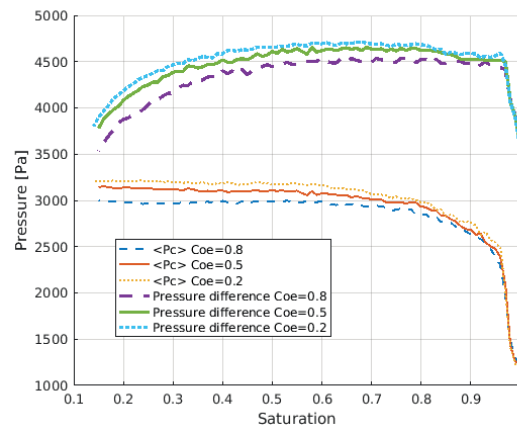


Fig. 3.4 Average phase pressure difference  $P^n - P^w$  and average capillary pressure  $P^c$  during drainage for different values of  $C_{oe}$

Drainage process for viscosity ratio of 1 is simulated with inlet non-wetting phase reservoir and outlet wetting phase reservoir pressure drop of 7000 Pa. Figure 3.4 gives

average phase pressure difference  $P^n - P^w$  and average capillary pressure  $P^c$  during drainage for different values of  $C_{oe}$ . Here average phase pressure is calculated based on equation (5.4) and average capillary pressure is calculated based on equation (3.28). Figure 3.5 shows saturation change over time for different values of  $C_{oe}$ . As can be seen, although difference exists between different values of  $C_{oe}$ , it may not be significant. Therefore, for simulations with large network, to improve computational time, a larger value of  $C_{oe}$  may be a reasonable choice.

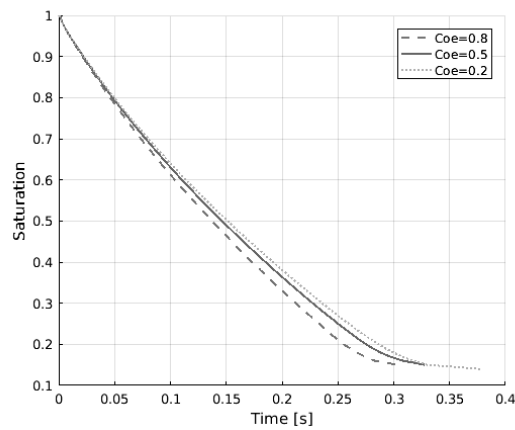


Fig. 3.5 Wetting phase saturation change with time during drainage for different values of  $C_{oe}$

#### Non-equilibrium effects in average phase pressure for different viscosity ratios

Figure 3.6 shows the average phase pressure difference  $P^n - P^w$  and average capillary pressure  $P^c$  during drainage for different values of viscosity ratio. Pressure difference between inlet non-wetting phase reservoir and outlet wetting phase reservoir is set to 8000 Pa. As viscosity ratio  $M$  decreases, the invasion front becomes more unstable. For a wetting phase saturation  $S^w$  of higher than 0.7, lower viscosity ratio in general has higher phase pressure difference. Later as invasion front develops, this is no longer the case. Figure 3.7 gives total saturation change over time during drainage for different viscosity ratios. Process involving more viscous fluid takes longer time.

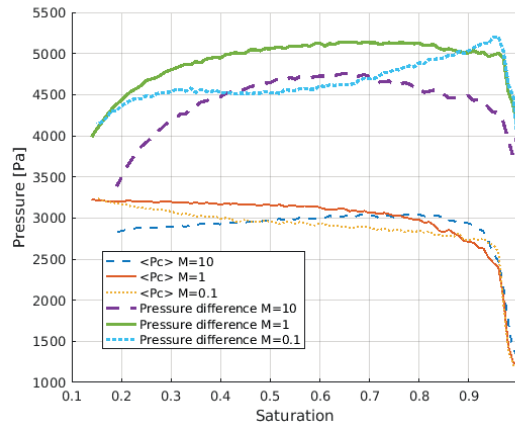


Fig. 3.6 Average phase pressure difference  $P^H - P^W$  and average capillary pressure  $P^C$  during drainage for different viscosity ratios

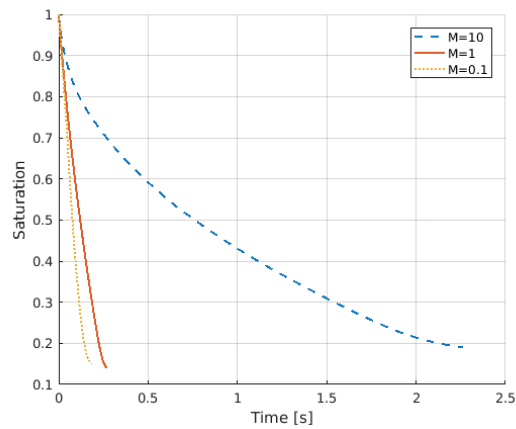


Fig. 3.7 Saturation change over time during drainage for different viscosity ratios

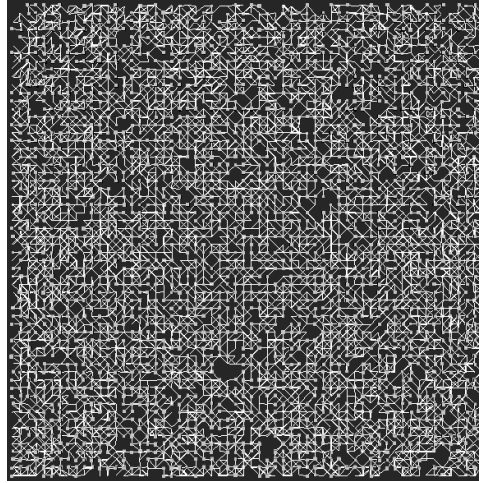


Fig. 3.8 Network used in simulations of saturation pattern in imbibition

### 3.3.4 Single-pressure imbibition: flow pattern for different boundary pressure drop

To compare different wetting advances during imbibition, we simulate imbibition into a two-layer network with statistical parameters given in Figure 4.1. Left side of network is connected with a wetting phase reservoir and the right side of network is connected with a non-wetting phase reservoir. Flow direction is from left to right. To have different Ca numbers, different boundary pressure drop,  $\Delta P = P_{inlet}^w - P_{outlet}^n$ , are used: (1)  $\Delta P = -1000$  Pa; (2)  $\Delta P = 0$  Pa (namely spontaneous imbibition); (3)  $\Delta P = 2000$  Pa.

Figure 3.9 gives saturation pattern change for these three different pressure drops. As we can see, for negative inlet/outlet pressure drop, invasion is more capillary dominant. With increase of inlet/outlet pressure drop, wetting front gets sharper, which is in quantitative agreement with reported experimental and numerical results (Hughes and Blunt, 2000; Lenormand et al., 1988).

## 3.4 Conclusion

A two-pressure dynamic drainage algorithm is developed for three-dimensional unstructured network model. Time step dependency is discussed through drainage simulations. Dynamic effects in average phase pressure for fluid pairs with different viscosity ratios are studied using the code as an upscaling tool. For cases where the two fluids have sig-

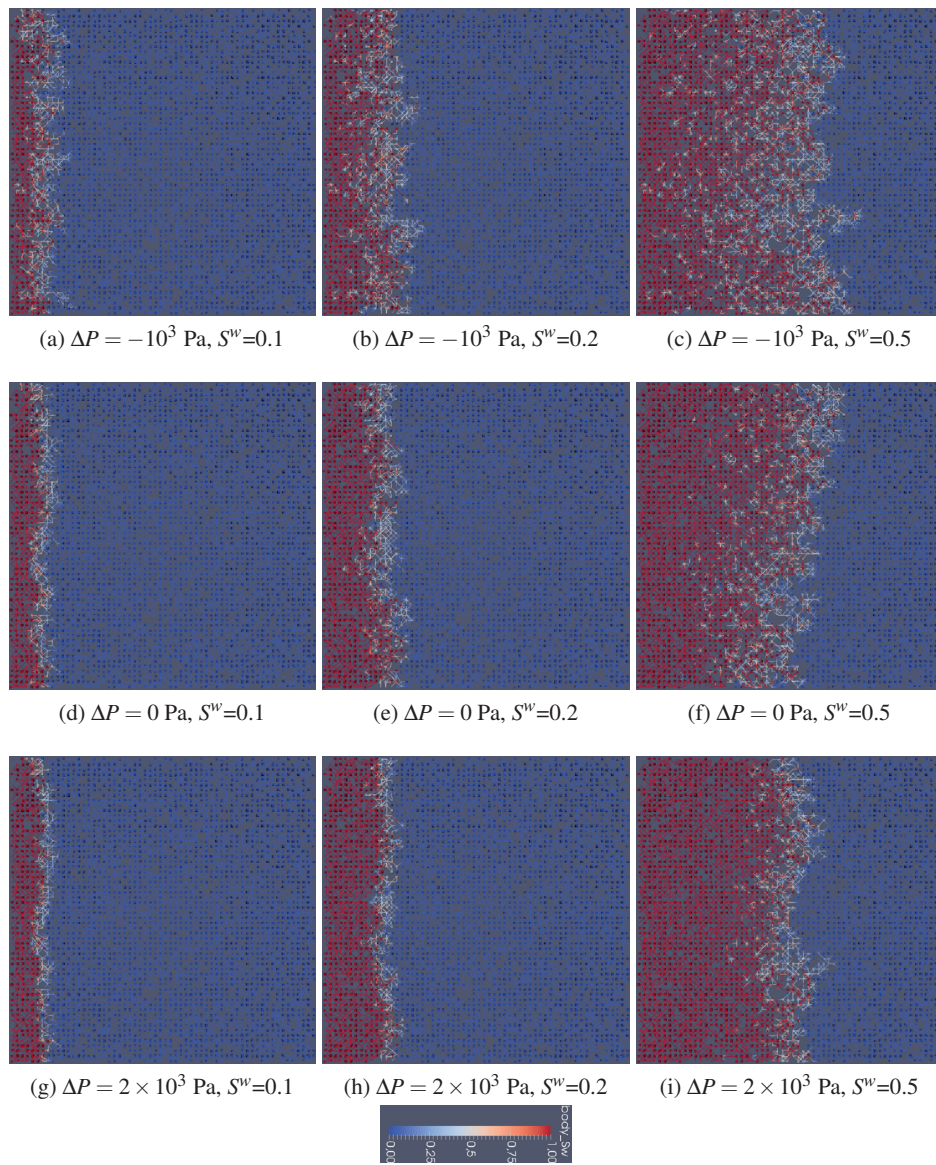


Fig. 3.9 Saturation pattern during imbibition for different boundary pressure drops

nificant viscosity difference, viscous pressure drop in one fluid may be negligible. This dynamic algorithm could be simplified to a single-pressure algorithm. Single-pressure algorithm for both drainage and imbibition are developed. Saturation pattern during imbibition for different boundary pressure drops are studied. With increase of boundary pressure, invasion becomes less capillary dominant and wetting front becomes sharper.

Our simulations show the efficiency and capacity of the developed models. These models can be employed in wider applications for study of two-phase flow in porous media.



## Chapter 4

# Droplet Imbibition into Paper Coating Layer: Pore-network Modeling Simulations

If you will tell me precisely what it is  
that a machine cannot do, then I can  
always make a machine which will do  
just that.

---

*John von Neumann*



## Abstract

Liquid penetration into thin porous media such as paper is often simulated using continuum-scale single-phase Darcy's law. The underlying assumption was that a sharp invasion front percolates through the layer.

To explore this ambiguous assumption and to understand the controlling pore-scale mechanisms, we have developed a dynamic pore-network model to simulate imbibition of a wetting phase from a droplet into a paper coating layer. The realistic pore structures are obtained using the FIB-SEM imaging of the coating material with a resolution of 3.5 nm. Pore-network structure was extracted from FIB-SEM images using Avizo software. Droplet sizes are chosen in the range of those applicable in inkjet printing. Our simulations show no sharp invasion front exists and there is presence of residual nonwetting phase. In addition, penetration of different sizes of droplets of different material properties into the pore network with different pore body and pore throat sizes are performed. We have found an approximately linear decrease of droplet volume with time. This contradicts the expected  $\sqrt{t}$ -behavior in vertical imbibition that is obtained using macroscopic single-phase Darcy's law.

Our simulations suggest that the single-phase Darcy's law does not adequately describe liquid penetration into materials such as paper coating layer. Instead Richards equation would be a better choice.

### 4.1 Introduction

The spreading and penetration of a liquid droplet into a porous layer is ubiquitous in industrial applications as well as natural systems. An important industrial example is the penetration of an ink droplet into paper during inkjet printing. Alongside viscous and capillary effects, many other phenomena may also be involved, such as evaporation, solidification, adsorption and diffusion. Research has been done to investigate the problem from experimental, theoretical, and/or numerical points of view. Reviews on

this topic can be found in Gambaryan-Roisman (2014), Daniel and Berg (2006), and Kettle et al. (2010).

For the study of spreading on a porous layer, much attention has been given to the droplet shape and size evolution, especially the physics taking place in the vicinity of the droplet edge (Alleborn and Raszillier, 2004; Anderson, 2005; Clarke et al., 2002; Davis and Hocking, 2000; Starov et al., 2002, 2003). Droplet-air interface is usually assumed to have a spherical or parabolic shape or it is modeled by lubrication theory.

Fluid behavior inside the porous medium is then interpreted based on droplet spreading information. In these studies, single-phase Darcy's law is often employed to model penetration inside porous media with underlying assumption of a sharp wetting front. For one-dimensional flow, this leads to the result that distance travelled by sharp wetting front varies with  $\sqrt{t}$ . For example, Lembach et al. (2011) visualized the transient spreading and infiltration of a droplet into a bed of transparent glass beads. Penetration depth and the information of the width of the front were obtained using image analysis. They employed single-phase Darcy's law to interpret their experimental measurements. A capillary pressure was assumed to act at wet/dry sharp boundary, and they addressed the important effect of dynamic contact angle assuming it to depend on the front velocity. However, the use of single-phase Darcy's law for description of droplet penetration into porous medium may be questioned as the underlying assumption of sharp wetting front may not always hold (Gambaryan-Roisman, 2014; Geiger and Durnford, 2000; Markicevic and Navaz, 2010).

Pore-scale simulation offers another approach to explore this process. Frank and Perré (2012) employed Lattice Boltzmann Method (LBM) to simulate droplet spreading over a hypothetical porous medium made of parallel vertical pores. Their numerical results showed power-law evolution of the wetted zone radius with time. They also discussed the competition between lateral spreading and capillary penetration. Meng et al. (2014) used Smoothed Particle Hydrodynamics (SPH) method to investigate main factors affecting the spreading process on a porous substrate including the contact angle, pore sizes and the gravity effects. The porous substrate is represented by a solid cube with square columns longitudinally penetrating the whole depth. Direct simulations in these studies often employ quite ideal regular geometry and topology and issues like dynamic contact angle and contact line pinning are not appropriately resolved.

A large body of works (Joekar-Niasar and Hassanizadeh, 2012b) exist for simulation of imbibition in porous media using pore-network models (Blunt, 2001; Blunt and Scher, 1995; Constantinides and Payatakes, 1996; Dias and Payatakes, 1986a,b; Hughes

and Blunt, 2000; Mogensen and Stenby, 1998; Nguyen et al., 2006). These single-pressure algorithms could suffer: (1) network with regular geometry/topology; (2) failure to include corner flow/film flow; (3) ignorance of capillary pressure at pores; (4) rule-based description of interface morphology; (5) rule-based dynamic algorithm.

In two-pressure algorithm, both pore body and pore throat can be filled with two fluids, each with its own pressure. Interface position or shape is not explicitly described but included in pore body capillary pressure-saturation relationship. Pressure, flux and saturation are calculated separately for each fluid. This algorithm was initially developed by Thompson (2002) for study of imbibition process in fibrous materials. Later this algorithm was improved and implemented onto structured network with fixed coordination number of six to study theories of two-phase flow in porous media (Joekar-Niasar and Hassanizadeh, 2011a,b; Joekar-Niasar et al., 2010) and wicking behavior (Joekar-Niasar and Hassanizadeh, 2012a). For two-phase flow involving two fluids with significant different viscosities, like water-air system, pressure drop in less viscous fluid may be negligible, and the above two-pressure algorithm may be simplified accordingly.

In this work, we have developed a dynamic single-pressure pore-network model to study the infiltration of a liquid into paper. Our model simulates the complex geometry and topology of the coating layer by constructing a network based on the statistical information obtained from a previous study using FIB-SEM imaging of a coating layer (Aslannejad et al., 2017). At this stage of the study, we only simulate the penetration of liquid inside the coating layer. So, the droplet evolution outside of the porous medium is not modeled, but it is considered as a known boundary condition.

The objectives of our study are as follows:

- 1) To develop a dynamic imbibition pore-network model and simulate a liquid penetration into the paper coating layer.
- 2) To study imbibition rate of different sizes of droplets and to explore the effects of the porous material properties and pore size.
- 3) To investigate displacement pattern during penetration and explore whether the sharp front assumption for liquid penetration is valid.

Paper coating layer properties are introduced in Section 4.2. The pore-network model is described in Section 4.3. Simulation results are shown and discussed in Section 4.4. Finally, the conclusions are provided in Section 4.5.

## 4.2 Properties of paper coating layer

### 4.2.1 Properties based on FIB-SEM image

Porosity of paper coating layer is about 0.34 and permeability is found to be 0.1 *mDarcy*, obtained by solving steady-state Stokes equations using Geodict(Math2Market, Kaiserslautern, Germany). More details can be found in Aslannejad et al. (2017).

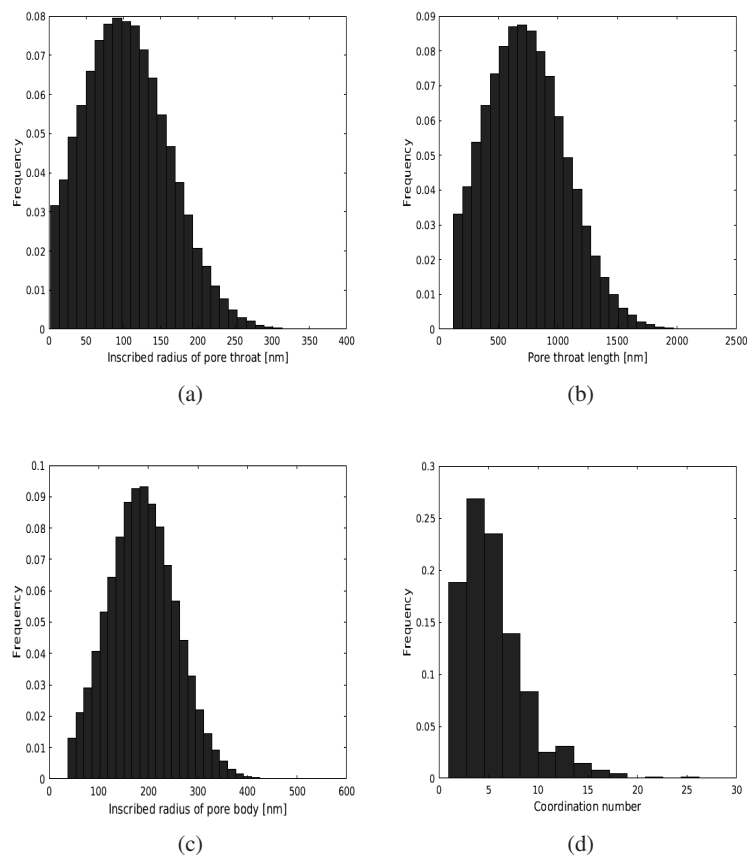


Fig. 4.1 Size distribution of (a) inscribed radii of pore throats; (b) pore throats length; (c) inscribed radii of pore bodies; (d) coordination number

Pore-network structure was extracted from FIB-SEM images using Avizo software (FEI Visualization Sciences Group). Figure 4.1 provides the size distribution of inscribed radii of pore throats, inscribed radii of pore bodies, length of pore throats and

Table 4.1 Material properties

Specification	Symbol	Value	Unit
Contact angle	$\theta$	45	degree
Interfacial tension	$\sigma^{wn}$	0.038 or 0.072	$kg s^{-2}$
Wetting fluid viscosity	$\mu^w$	0.001 or 0.040	$kg m^{-1} s^{-1}$

coordination number. These data will be used later in Section 4.3 to construct the pore network.

### 4.3 Pore-network model description

Details about single-pressure algorithm for imbibition can be found in Chapter 3.

#### 4.3.1 Model features

**Structure and geometry** The pore network is generated using an irregular network generator developed by Raoof and Hassanizadeh (2012). Pore bodies are considered to have a cubic shape and pore throats are assigned square cross sections. Pore body and pore throat sizes distribution and coordination number distribution are shown in Figure 4.1. Porosity of the network is 0.37, close to that of 0.34 of the sample. Intrinsic permeability of the generated pore network is found to be 0.12 *mDarcy*, which compares well with 0.1 *mDarcy* obtained using image- based direct simulations. This shows that the extracted pore structures are representative of the coating layer. To explore effects of pore body and pore throat sizes on imbibition, we simulate two different scenarios: (1) G1: based on sizes distributions shown in Figure 4.1; (2) G2: the same distribution as G1 but increasing pore body and pore throat sizes by a factor of 2; keeping coordination number distribution unchanged.

**System parameters** Table 4.1 gives fluid properties used in the simulations. Contact angle value is taken from Aslannejad et al. (2017). Two sets of material properties are adopted: (1) M1: interfacial tension is 0.072  $kg s^{-2}$  and wetting phase viscosity is 0.001  $kg m^{-1} s^{-1}$ ; these values correspond to water-air system. (2) M2: interfacial tension is 0.038  $kg s^{-2}$  and wetting phase viscosity is 0.040  $kg m^{-1} s^{-1}$ ; these values correspond to a glycerol solution used in Clarke et al. (2002).

## 4.4 Dynamic simulation results and discussion

In inkjet system, the droplet volume typically ranges from  $4 pL$  to  $18 pL$  ( $pL = \text{picoliter}$ ) with minimum droplet size of  $2 pL$  (Clarke et al., 2002; Kettle et al., 2010). We simulate for different droplet sizes of  $2 pL$ ,  $4 pL$ ,  $8 pL$ ,  $12 pL$ , each penetrating into two different pore networks (G1, G2) with material properties (M1, M2), details about (G1, G2) and (M1, M2) is given in Section 4.3.

### 4.4.1 Symmetry of saturation pattern during droplet penetration

For a big droplet, the simulation of a big domain will be needed which would be extremely time consuming. One way to reduce the computational time is to simulate only part of the domain, considering the symmetric development of macroscopic saturation pattern. We will simulate a  $2 pL$  droplet penetration first and check the symmetry of the resulting pore-scale saturation pattern. Based on the results, we determine the domain size of our simulations. The coordinate system is chosen so that the inlet is in the  $x - y$  plane.

Figures 4.2 (a) – (f) and Figures 4.3 (a) – (f) give the cross-sectional view and top layer of saturation pattern development in the full domain during a  $2 pL$  droplet penetration. As the saturation pattern develops, it becomes less symmetric due to the heterogeneity of pore network. Nevertheless, Figures 4.2 and 4.3 show that the main features of the process can be captured for simulation on  $1/4$  of the domain.

Therefore, in our dynamic simulations, we simulate  $1/4$  of the domain, namely penetration of  $1/4$  of a droplet into the porous medium. Domain size will be chosen so that no breakthrough happens at any faces of the domain. So, for simulation of droplets of different sizes, different domains sizes may have been chosen.

### 4.4.2 Penetration time

**Dynamics of droplet volume with time** As a droplet imbibes into a porous medium, its volume decreases. Based on fluxes, we can calculate the change of its volume over time. Figure 4.4 shows the volume change as function of time for a  $2 pL$  droplet obtained from simulations using two different domain sizes:  $1/4$  domain and full domain. Volumes are normalized to their initial values. Good agreement between these two simulations further confirms the adequacy of simulations for  $1/4$  of a droplet. In addition, we observe a linear decrease of droplet volume with time.

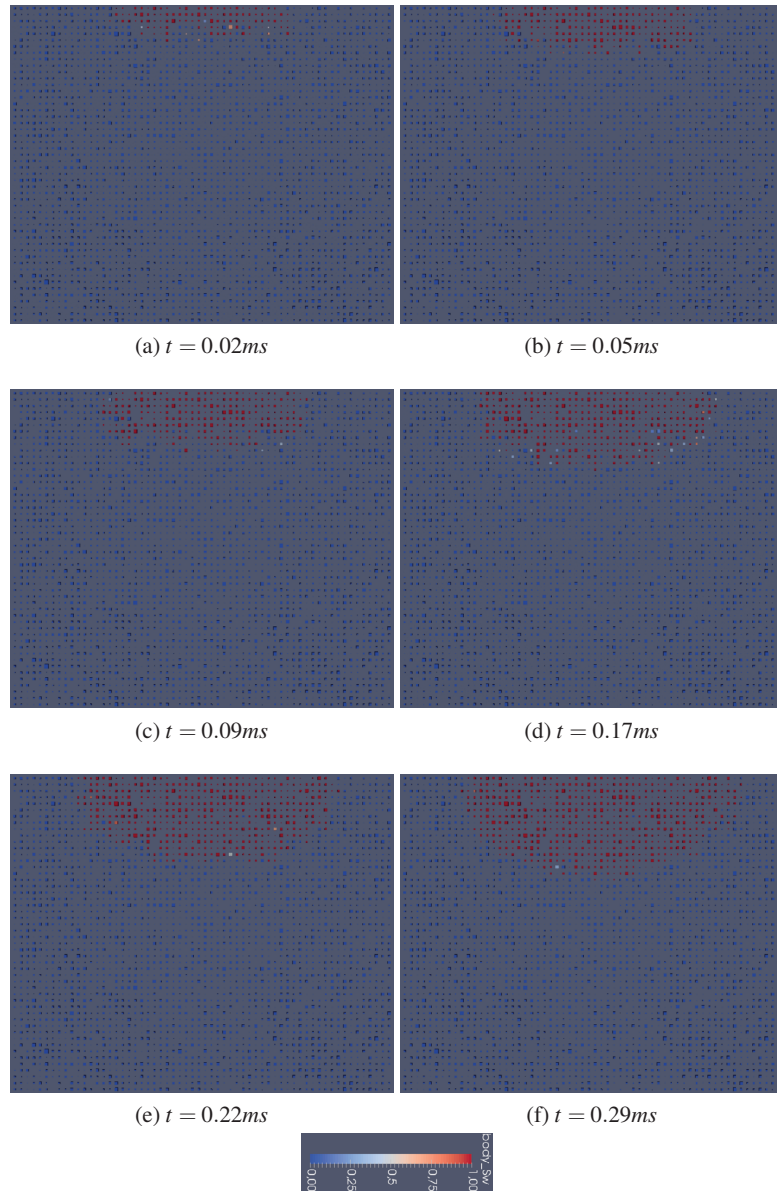


Fig. 4.2 Cross-sectional view of the pore-scale saturation pattern evolution with time during the penetration of a  $2 pL$  droplet (diameter of  $16\mu m$ , pore network G1, material properties M1)

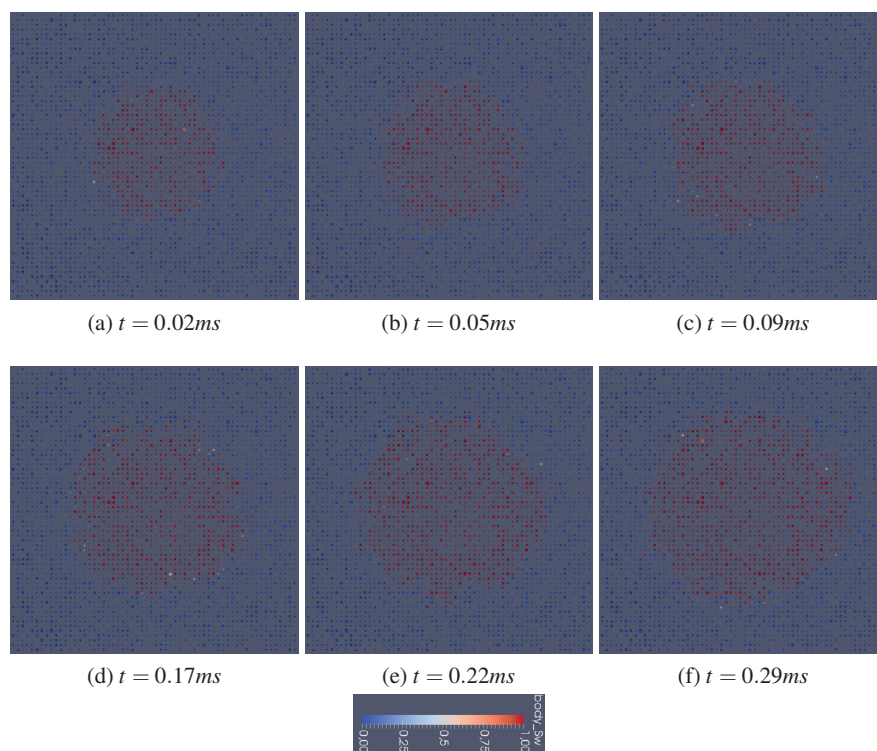


Fig. 4.3 Top layer of the saturation pattern evolution from (a) to (f) during a  $2 pL$  droplet penetration (diameter of  $16\mu m$ , pore network G1, material properties M1)

Using a picoliter spreading and absorption instrument, Clarke et al. (2002) found that a glycerol solution droplet took around 10 to 80ms for about 90% of its initial volume to penetrate. Moreover, similar to our simulation, linear decrease of droplets volume with time was observed. Droplets in their experiments had a volume around 100 pL and four types of porous media with minimum pore sizes of 100nm, 220nm, 450nm, 650nm were used. Interfacial tension was  $0.038 \text{ kgs}^{-2}$  and wetting phase viscosity was  $0.040 \text{ kgm}^{-1}\text{s}^{-1}$ ; the contact angle value was not reported.

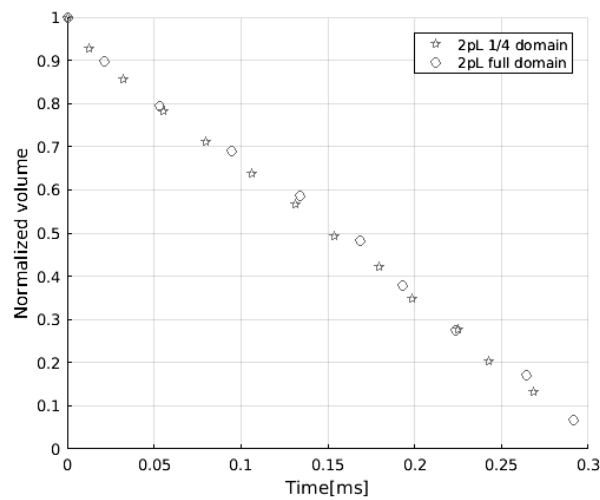


Fig. 4.4 Variation of droplet volume as function of time for a 2 pL droplet in 1/4 domain and full domain (diameter of  $16\mu\text{m}$ , pore network G1, material properties M1)

Figures 4.5 and 4.6 show droplet volume change with time for different droplet sizes and material properties. As expected, we can see that bigger droplets take longer to imbibe into the porous medium. Also, lower interfacial tension and higher viscosity decrease imbibition rate. We find a linear decrease of droplets volume with time as was observed by Clarke et al. (2002). This results contradict the  $\sqrt{t}$  trend that one obtains from macroscale simulations based on single-phase Darcy's law. This may, on one hand, be due to the important effect of radial flow; on the other hand, be due to the failure of single-phase Darcy's law for this possible two-phase problem.

**Effects of pore size on penetration time** We simulated penetration of different sized droplets into the pore networks G1 and G2 using material properties set M1. Figure 4.7 shows, as expected, how imbibition rate increases with increase in pore sizes. This is

54 | Droplet Imbibition into Paper Coating Layer: Pore-network Modeling Simulations

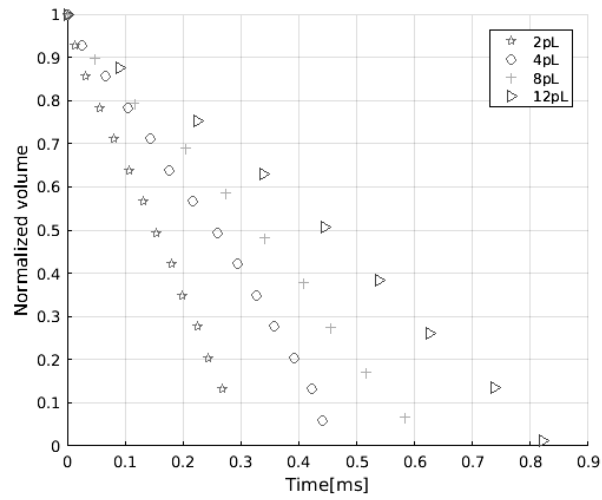


Fig. 4.5 Variation of droplet volume as function of time for different droplet sizes (pore network G1, material properties M1)

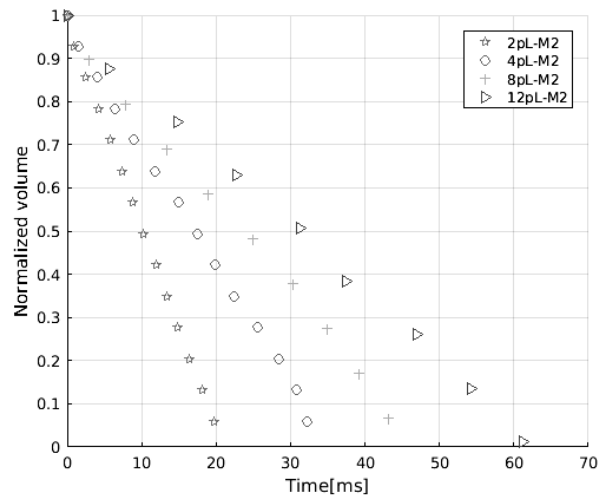


Fig. 4.6 Variation of droplet volume as function of time for different droplet sizes (pore network G1, material properties M2)

in agreement with experimental results in Clarke et al. (2002) and agrees well with Lucas-Washburn equation for a capillary tube. Moreover, we find a linear decrease of droplet volume with time even for larger pore sizes.

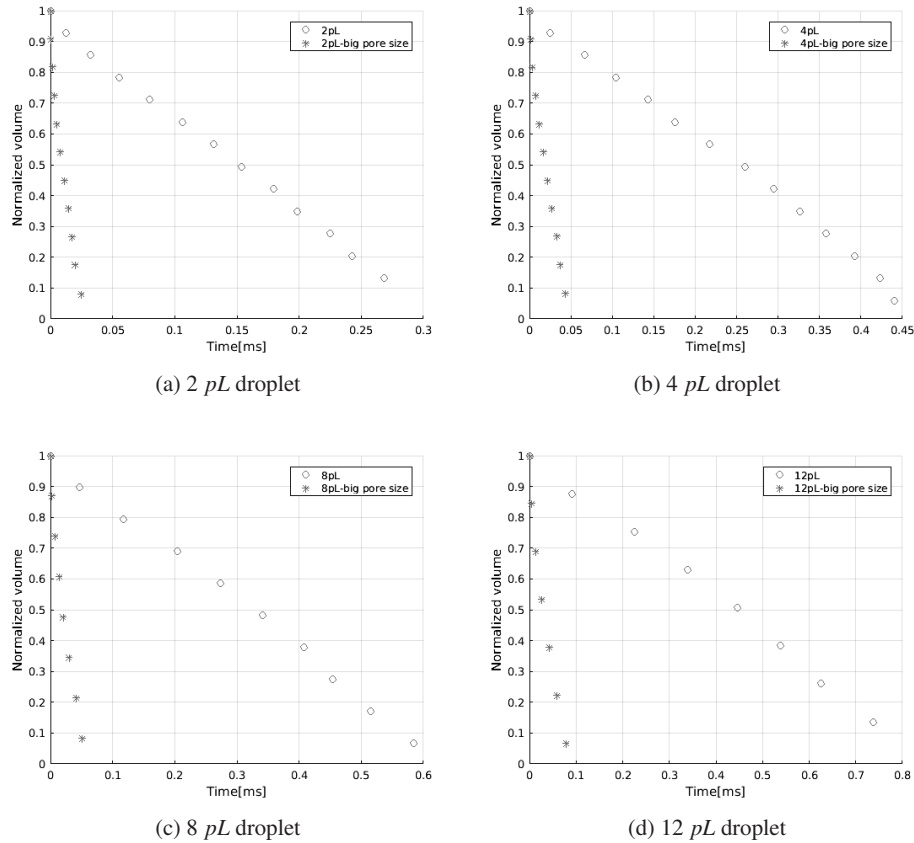


Fig. 4.7 Effect of pore size on droplet volume change over time for droplets of different sizes (material properties M1): (a) 2 pL droplet; (b) 4 pL droplet; (c) 8 pL droplet; (d) 12 pL droplet.

#### 4.4.3 Invasion pattern

In this section, we would like to explore whether a sharp invasion front exists during droplet penetration. We will check the invasion pattern just after droplet has fully penetrated into the porous medium. Simulations are performed on pore network G1 using material properties M1 and M2.

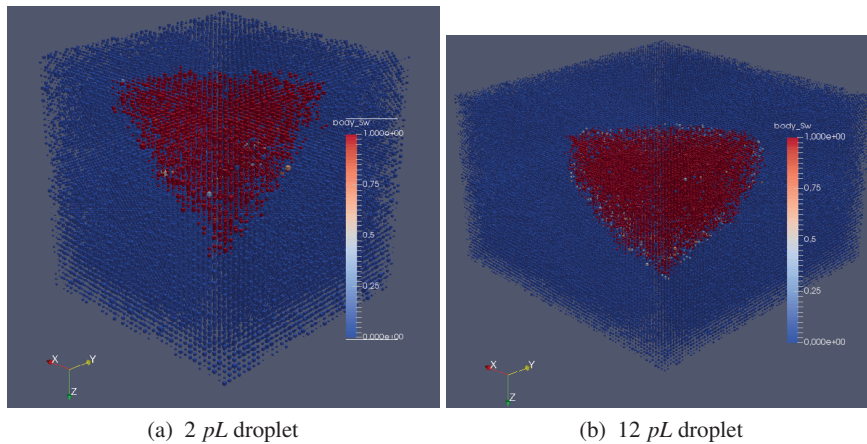


Fig. 4.8 Saturation pattern just after a droplet has fully penetrated into porous medium (material properties M1) (a) 2 pL droplet (b) 12 pL droplet.

Figure 4.8 provides a 3D view of the saturation patterns for droplets of 2 pL and 12 pL and Figures 4.9 - 4.11 show the top and side views of the saturation pattern for different droplet sizes with different material properties. For smaller droplet, saturation front is more sharper. Due to presence of small pore sizes together with pressure conditions at the boundaries, displacement is more piston-like and snap-off is suppressed (Hughes and Blunt, 2000). Still as we can see no sharp invasion front exists and the nonwetting phase stays behind the front; this effect cannot be accounted for by single-phase Darcy's law model of liquid penetration in porous media. Conceptually, Richards equation provides a better choice (Bear, 1972; Markicevic and Navaz, 2010). However, this requires knowledge of macroscopic properties, like capillary pressure-saturation relationship, relative permeability, which may be difficult to determine accurately.

## 4.5 Conclusion

In this work, we have developed a single-pressure dynamic pore-network model for primary imbibition and applied it for simulation of a droplet penetration into the coating layer of a coated paper. The model is based on an explicit-saturation implicit-pressure algorithm. However, it is made specially fast by solving pressure for fully wetting phase saturated pore bodies only. Geometry and topology of the pore network are based on FIB-SEM image of the coating material. Penetration of different sizes of droplets of

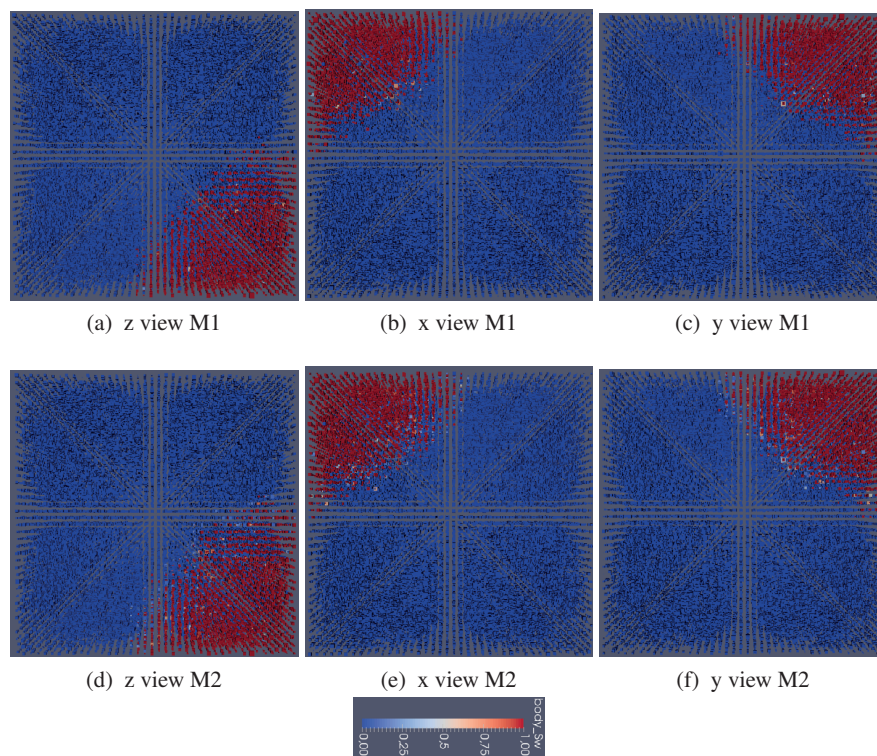


Fig. 4.9 Top ( $z$ ) and side ( $x, y$ ) view of the saturation pattern of  $2 pL$  droplet for different material properties ((a)-(c): M1; (d)-(f): M2).

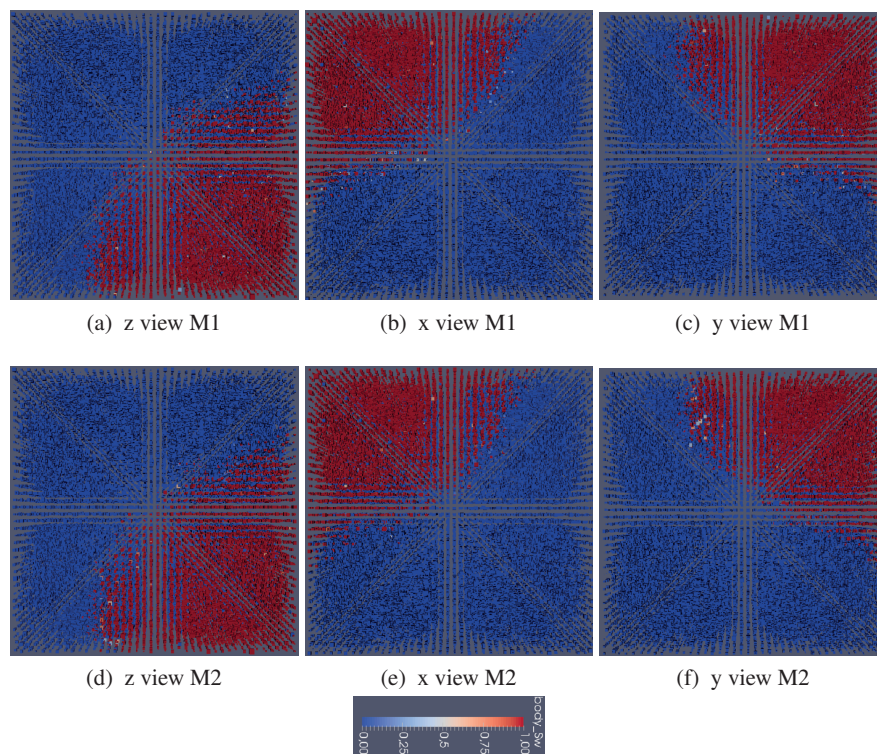


Fig. 4.10 Top ( $z$ ) and side ( $x,y$ ) view of the saturation pattern of 4  $pL$  droplet for different material properties ((a)-(c): M1; (d)-(f): M2).

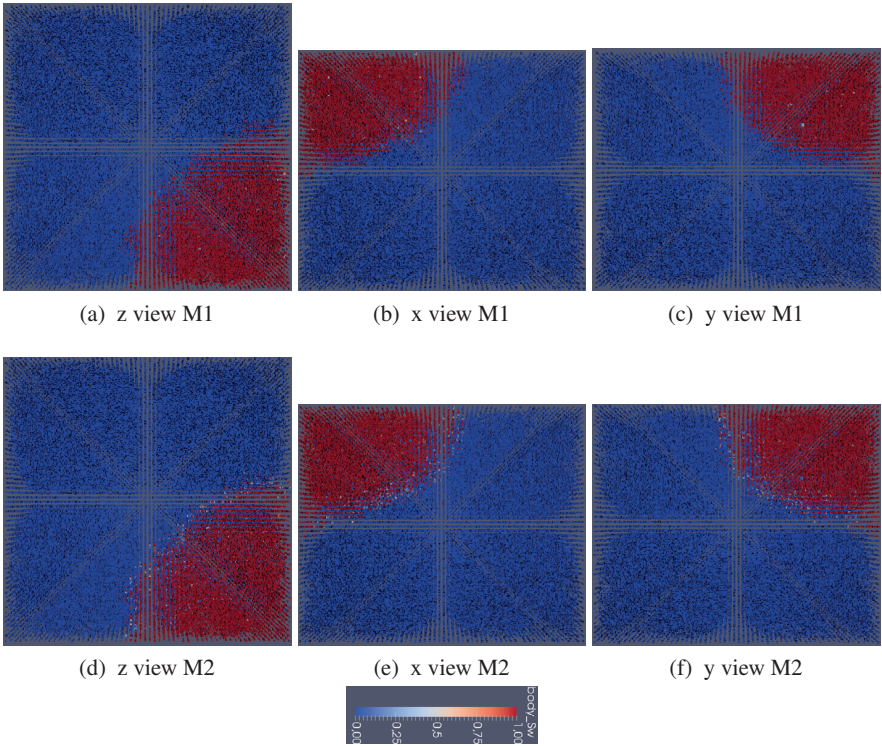


Fig. 4.11 Top ( $z$ ) and side ( $x,y$ ) view of the saturation pattern of 8  $pL$  droplet for different material properties ((a)-(c): M1; (d)-(f): M2).

## 60 | Droplet Imbibition into Paper Coating Layer: Pore-network Modeling Simulations

---

different material properties into pore network of different geometries are performed. Droplet sizes are comparable with those of real inkjet droplets. Simulations show a linear decrease of droplet volume with time, and this contradicts the expected  $\sqrt{t}$ -behavior in vertical imbibition that is obtained using macroscopic single-phase Darcy's law. This discrepancy is partly due to the important effect of radial flow and partly due to the inadequacy of single-phase Darcy's law for such two-phase flow problem.

The examination of saturation patterns obtained from our simulations shows that no sharp invasion front exists and there is presence of (residual) nonwetting phase behind the front. This means single-phase Darcy's law is not appropriate for macroscale simulation of liquid penetration under these conditions. It is expected that Richards equation would be a better choice (Bear, 1972; Markicevic and Navaz, 2010), although one needs to deal with more complex properties, like capillary pressure-saturation relationship, relative permeability, which may be difficult to measure.

Future work is needed to incorporate the spreading of droplet on the surface of the porous substrate and couple the spreading and penetration process. Also wetting phase behavior inside the porous medium after complete penetration of droplet should be studied. In this study, pure liquids have been the working fluids. Description of dye-based or pigment-based colorant movement should also be incorporated using more complex models.

## Chapter 5

# Pore-network Modeling of Dynamic Capillarity Effect during Fast Drainage in Sandbox Experiments

The true laws can not be linear nor  
can they be derived from such.

---

*Albert Einstein*



## Abstract

A dynamic single-pressure pore-network model is developed and employed for simulating dynamic capillarity effect during fast drainage in sandbox experiments. Saturation and water pressure were recorded during the experiment. Pore network is constructed such that it matches the porosity, intrinsic permeability and quasi-static  $P^c - S^w$  curve from experimental measurements. Single-pressure algorithm is adopted considering negligible viscosity of air compared with that of water. Scale dependence of dynamic capillarity coefficient  $\tau$  has been discussed through numerical simulation. Our simulation results match the change of average  $\frac{dS^w}{dt}$ . Values of  $\tau$  calculated based on numerical simulations are in the same order as those obtained from experimental results. Also, a similar trend of  $\tau$  dependence on saturation is found between numerical and experimental results. Simulations show the ability of our pore-network model to simulate dynamic experiments.

## 5.1 Introduction

### 5.1.1 Use of dynamic pore-network models for simulating experiments

Pore-network models can be categorized as quasi-static or dynamic. Quasi-static models have been successfully employed for the prediction of relative permeabilities and capillary pressure-saturation relationship in multiphase system (Joekar Niasar et al., 2009; Oren et al., 1998; Patzek, 2001; Piri and Blunt, 2005).

A dynamic pore-network model has to be employed when viscous forces need to be considered together with capillary force. Comprehensive reviews can be found in Joekar-Niasar and Hassanizadeh (2012b), as well as Aghaei and Piri (2015). There are still limited works on simulating dynamic experiments employing pore-network models, where experimental network structure, initial condition and boundary condition are properly implemented and pore-network model simulations are compared with experimental observations. Below we review some of them.

## 64 | Pore-network Modeling of Dynamic Capillarity Effect during Fast Drainage in Sandbox Experiments

---

Lenormand et al. (1988) performed drainage simulations and found similarity between experimental and simulated flow patterns and cross-over between different flow patterns zones. They mapped these different flow patterns onto the plane of capillary number and viscosity ratio. No attempt was made to represent the experimental domain (size) and pore geometry in numerical simulator. So they only found qualitative agreement with experimental results.

van der Marck et al. (1997) extended the numerical pore-network model of Lenormand et al. (1988).

Depth of network in numerical simulator was checked and tuned based on single phase pressure-flow rate correspondence with experiment. They compared pressure buildup at boundary and saturation in the domain before breakthrough during flow controlled drainage process. Good agreement was found for case with viscosity ratio as 1 while discrepancy existed when nonwetting phase is much more viscous than wetting phase. No corner flow or film flow was included in their model.

Aker et al. (1998) modeled the dynamics of drainage dominated flow where film flow can be neglected using a two-dimensional network simulator. Simultaneous flow of two liquids into one tube was allowed. The flow front width from simulation was found to be consistent with a scaling relation and scaling exponents were compared with experimental data from the literature.

Singh and Mohanty (2003) developed a rule-based dynamic network model to simulate two-phase flow in three-dimensional porous media. Film flow has been incorporated. Capillary desaturation curves and dependence of relative permeability upon saturation were in good qualitative agreement with literature experimental results.

Nordhaug et al. (2003) used a dynamic network model to provide upscaled variables: interfacial area in the averaging volume and average interfacial velocity. To validate their network code against sand column experiment, a network was constructed based on the monodisperse sphere packing model. Interfacial area-saturation curve was in good agreement with experimental findings.

Løvoll et al. (2005) simulated the displacement of a highly viscous wetting fluid by a non-wetting fluid with low viscosity in a porous medium of a single layer of glass beads under stabilizing gravity. The porous medium was represented numerically by a two-dimensional square network of tubes inclined at a 45 degree angle. Consistency in scaling of the front width as a function of the generalized Bond number for the experiments and numerical simulations was found.

Nguyen et al. (2006) developed a dynamic network model for imbibition based on a physically realistic description of the complex dynamics of film flow, film swelling and snap-off. Relative permeability curves and residual oil saturation data under different displacement rates were compared with experimental data reported in literature.

Karpyn and Piri (2007), Piri and Karpyn (2007) generated a two-dimensional pore-scale network model of a rough-walled fracture whose inner structure had been mapped using X-ray microtomography. The model consisted of a rectangular lattice of conceptual pores and throats representing local aperture variations. Both primary and secondary drainage results revealed excellent agreement with X-ray CT slices showing fluid occupancy at various fracture locations.

Tørå et al. (2012) presented a dynamic network model that can handle both drainage, imbibition, and steady-state displacement. They found saturation profiles for imbibition in qualitative agreement with experiments reported in literature.

DiCarlo (2006) employed a physically based network model (Valvatne and Blunt, 2004; Valvatne et al., 2005) to simulate saturation overshoot experiments (DiCarlo, 2004). Viscous effects are added in the model quasi-statically to allow computations on a large network for comparisons with experiments. Quantitative discrepancy in oversaturation magnitudes was found between simulation and experiments.

Aghaei and Piri (2015) presented a dynamic pore-network model that is capable of up-scaling two-phase flow processes from pore to core. The dynamic model was validated by comparing the predicted local saturation profiles, fractional flow curves, relative permeabilities, and residual oil saturations against experimental counterparts in core-flooding experiments. Due to the failure of the pressure transducers during experiment, no comparison of pressure drop data was made.

### 5.1.2 Dynamic capillary effect

Capillary pressure is a fundamentally important concept in classical modeling of multiphase flow in porous media. The capillary pressure-saturation relationship is needed to close the system of equations for multiphase flow. This equation is commonly written as:

$$P^c = P^n - P^w = f(S^w) \quad (5.1)$$

where  $P^c$  is capillary pressure,  $P^\alpha$  is pressure of  $\alpha$  phase and  $S^\alpha$  is saturation of  $\alpha$  phase.

## 66 | Pore-network Modeling of Dynamic Capillarity Effect during Fast Drainage in Sandbox Experiments

In this classical description, there is no difference between capillary pressure and pressure difference of non-wetting phase and wetting phase. Experiments have shown that above capillary pressure-saturation relationship only applies under equilibrium conditions (see detailed review in Hassanizadeh et al. (2002)). A theoretical thermodynamic basis of capillary pressure is laid and a linear approximation has been given for this dynamic capillary effect (Hassanizadeh and Gray, 1990, 1993), in the following form:

$$P^n - P^w = P^c - \tau \frac{\partial S^w}{\partial t} \quad (5.2)$$

where  $\tau$  is called dynamic capillary coefficient. Magnitude of  $\tau$ , dependence of  $\tau$  on system properties, and scale-dependence of  $\tau$  have been subjects of many experimental and numerical works (Abidoye and Das, 2014; Bottero et al., 2011; Camps-Roach et al., 2010; Das et al., 2014; Das and Mirzaei, 2012; Hassanizadeh et al., 2002; Hou et al., 2012; Joekar-Niasar and Hassanizadeh, 2012b; O'Carroll et al., 2005; Sakaki et al., 2010).

### 5.1.3 Aims and scopes

With development of imaging techniques and micro-fluidics experiments, it has become possible to compare details of pore-network model simulations with experimental findings. To investigate Equation (5.2), a dynamic pore-network model has been developed and employed to simulate real experiment and investigate dynamic capillarity effect. So objective of this work is to:

- (1) develop a dynamic single-pressure pore-network model;
- (2) employ this model for simulation of sandbox experiments to study dynamic capillarity effect.

## 5.2 Experimental setup and procedure

Experiments reported and studied here were performed by Zhuang et al. (2017), who provide full details. Here, we give a short description of experiments. The experiments were designed to investigate dynamic effect and the hysteretic behavior of dynamic capillarity coefficient  $\tau$  in Equation (5.2) during air-water two-phase flow.

Experiments were conducted using a custom-built Plexiglas sandbox. A schematic view of the experimental setup is shown in Figure 5.1 . The height of the sandbox was 3 cm and has a cross section of 3 cm by 2 cm. A valve at the top of sandbox (Valve 1)

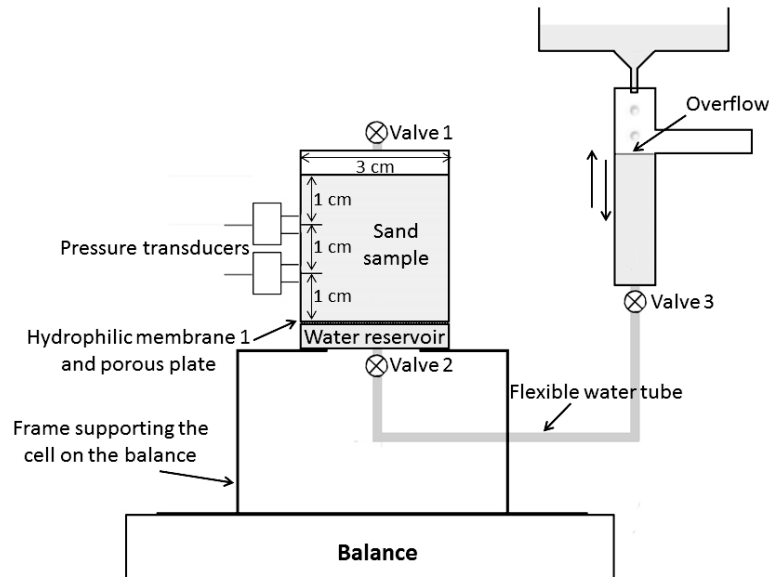


Fig. 5.1 Schematic diagram of experimental setup

was connected to a sealed balloon, filled with moist air. At the bottom of sandbox a hydrophilic nylon membrane (mean pore size,  $5 \mu\text{m}$ ) was used, to serve as a capillary barrier to air. The water reservoir at the bottom of setup was connected to a small water column using a flexible tube. The hanging water column which was used to control water pressure head at the outlet. The entire sandbox was placed on a 3-digit precision balance. Readings of the balance were used to calculate changes in average saturation of the sandbox.

Two pressure transducers were installed at depths of 1 and 2 cm of the sandbox. The dead volume of the transducer was saturated with water before installation. The transducer was connected to the side wall of the sandbox, with an opening of 5 mm in diameter. A hydrophilic membrane with a mean pore size of  $0.45 \mu\text{m}$  was adhered to the opening of the inner wall of the sandbox and covering the opening. The membrane was saturated with degassed water in all experiments. This membrane ensured that no air would enter the transducer dead volume. The response time of the transducers was determined to be 0.4 seconds.

In quasi-static experiments, at first, the hanging water column was kept at the bottom of the sand sample. Valve 2 and Valve 3 (see Figure 5.1) were always open. The elevation of the hanging column was decreased in small increments. The readings from

## 68 | Pore-network Modeling of Dynamic Capillarity Effect during Fast Drainage in Sandbox Experiments

---

pressure transducers were monitored to ensure that the equilibrium was established at each elevation.

In the dynamic primary drainage experiments, the saturated sand sample was first drained under quasi-static conditions. After reaching a certain water saturation and pressure (serving as the initial conditions for subsequent dynamic experiments), Valve 3 was closed and the hanging water column was lowered to  $-70$  cm  $H_2O$  below the bottom of the sandbox. Dynamic drainage experiments started by opening Valve 3. This resulted in a rapid drainage of the sand box. Local water pressures and average water saturation were collected every  $0.5$  s for a maximum of  $4000$  s. As dynamics of the system decrease quickly, for primary drainage, only data of first  $140$  s were used (roughly corresponding to  $S^w$  range  $0.6$ - $0.83$ ) for the calculation of dynamic capillarity coefficient  $\tau$ .

### 5.3 Pore-network model description

Details about the single-pressure algorithm for drainage can be found in Chapter 3.

#### 5.3.1 Model features

**Structure and geometry** Pore bodies are all given a cubic shape and pore throats have square cross sections. The unstructured pore network is generated by a network generator developed by Raoof and Hassanizadeh (2012). One can assign a prespecified average coordination number to the network, with coordination number of individual pore bodies varying between 1 and 26. Pore bodies size distribution, pore throats size distribution, average coordination number are tuned based on soil grain size distribution, porosity, intrinsic permeability and quasi-static Pc-S curve from experimental measurements. Details are given in Section 5.4. Figure 5.2 provides the distribution of inscribed radii sizes of pore throats, inscribed radii sizes of pore bodies, length sizes of pore throats and coordination number.

**System parameters** Table 5.1 gives fluid properties used in the simulation.

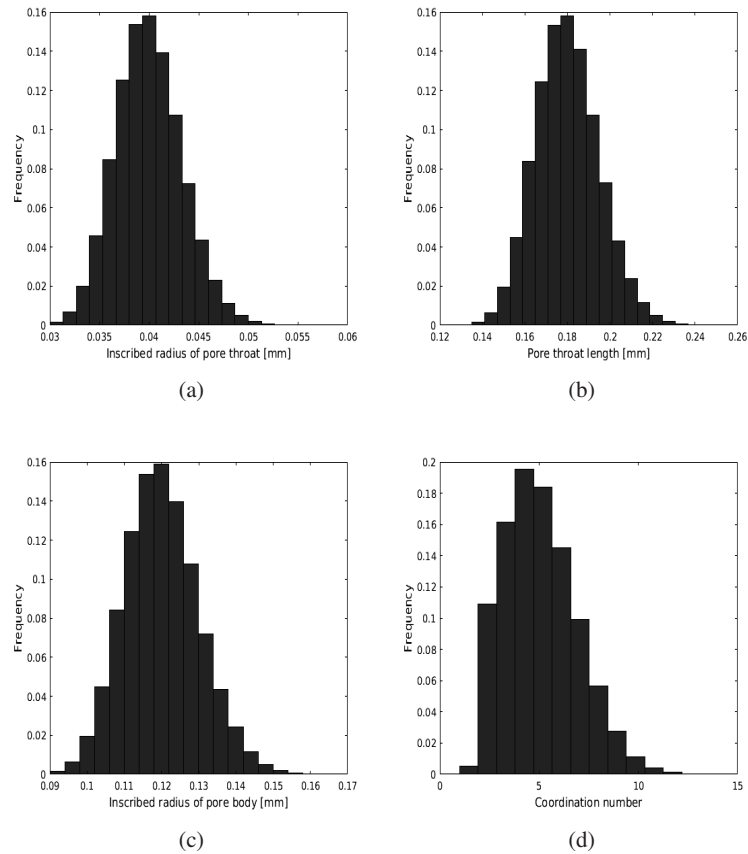


Fig. 5.2 Distribution of (a) inscribed radii of pore throats; (b) pore throats length; (c) inscribed radii of pore bodies; (d) coordination number

Table 5.1 Material properties

Specification	Symbol	Value	Unit
Contact angle	$\theta$	17	degree
Water-air interfacial tension	$\sigma^{wn}$	0.072	$kg s^{-2}$
Water viscosity	$\mu^w$	0.001	$kg m^{-1} s^{-1}$
Water density	$\rho^w$	1000	$kg m^{-3}$

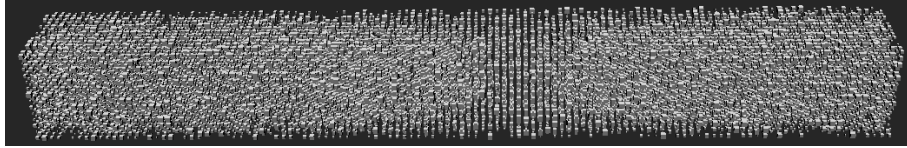


Fig. 5.3 Network for sandbox experiments simulations

## 5.4 Simulation results and discussion

### 5.4.1 Computational domain, boundary and initial conditions

The flow in the sandbox could be considered as a one-dimensional vertical drainage of water. The sandbox is simulated by a large network with lattice size of  $120 \times 14 \times 14$ , and pore bodies at some lattice positions are deleted based on network generation algorithm (Raouf and Hassanizadeh, 2012) resulting 22165 pore bodies in total. Porosity of the pore network was 0.41, which is in good agreement with the sand packing porosity of 0.39. One face of the network is connected with inlet reservoir and the other face is connected with outlet reservoir. Closed boundary condition is imposed at side boundary. Intrinsic permeability of the pore network was calculated to be  $1.69 \times 10^{-11} m^2$ , which compares well with the measured permeability of  $1.7 \times 10^{-11} m^2$ .

In the simulation, inscribed radius of pore throats connected with outlet reservoir are reduced by a factor of 7. In this way, we try to recover the effects of the experimental hydrophilic nylon membrane at outlet: capillary barrier effect and viscous effect.

As explained earlier, in the dynamic drainage experiment, the saturated sample was first drained quasi-statically to a saturation lower than 100% and then dynamic drainage was started. So in our simulations, we first did quasi-static primary drainage to reach almost the same average saturation as in the experiment. The state of pores occupancy obtained from quasi-static simulation then was used as initial condition for dynamic simulations.

### 5.4.2 Averaging of pore-network simulation data

Pore-network simulations produce pore-scale information on pressure and saturation in pore bodies. These pore-scale values were averaged over a large number of pore bodies in order to obtain macroscale quantities. These were obtained from the following intrinsic volume averaging definitions:

$$S^\alpha = \frac{\sum_{i=1}^{N_b} s_i^\alpha V_i}{\sum_{i=1}^{N_b} V_i}, \alpha = n, w \quad (5.3)$$

$$P^\alpha = \frac{\sum_{i=1}^{N_b} p_i^\alpha s_i^\alpha V_i}{\sum_{i=1}^{N_b} s_i^\alpha V_i}, \alpha = n, w \quad (5.4)$$

where  $N_b$  denotes the total number of pore bodies within the averaging domain. We are aware that this definition of average pressure may result in numerically-enhanced dynamic effect (Korteland et al., 2010; Nordbotten et al., 2007, 2008). Nevertheless, we follow the usual practice in the definition of average pressure. With regard to the averaging domain, we chose two different sizes: (1) the whole network representing the sandbox; (2) the middle 1/3 of the network, representing the domain between the two transducers, see Fig.(5.1) .

### 5.4.3 Quasi-static simulation of $P^c$ - $S^w$ curves

Figure 5.4 shows comparison of quasi-static  $P^c$ - $S^w$  curves from pore-network simulation and experiment. This comparison further shows the adequacy of our network to mimic the sand sample.

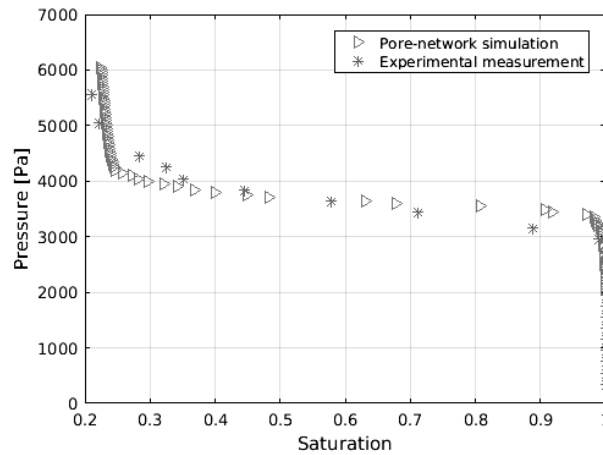


Fig. 5.4 Quasi-static  $P^c$ - $S^w$  comparison between simulation and experiment

#### 5.4.4 Dynamic simulation

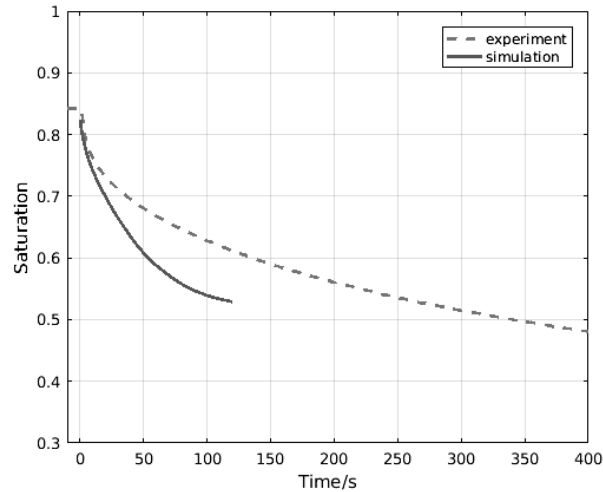


Fig. 5.5 Global saturation change with time: comparison between simulation and experimental measurement

**Change of average saturation with time** In the experiment, only the saturation averaged over the whole sandbox was measured as a function of time. Experimental results are compared with results of our simulations in Figure 5.5. Note that simulation had to be stopped as the runtime was becoming prohibitive at low flow rate (drainage was coming to an end). This was not considered to be a major shortcoming as the calculation of  $\tau$  from experimental data was based on saturation values above 0.6.

As we can see from Figure 5.5, simulated saturation changes is about 2 or 3 times faster than measured values. Also we observe the decrease of the dynamics of the system with time, change of saturation becomes weaker as invasion happens. Figure 5.6 shows saturation change rate  $\frac{dS^w}{dt}$  from simulation, using backward difference approximation, in comparison with experimental measurement. In our simulation, in general we have monotonic change of  $\frac{dS^w}{dt}$  with saturation.

**Scale dependence of dynamic capillarity coefficient  $\tau$**  As we mentioned earlier, in the experiments, pressure was measured locally at two locations in the sandbox (depth of 1 cm and 2 cm) whereas saturation was measured as an average value for the whole sandbox. So in the interpretation of data, in order to have consistency in scale, pressure measured by the two transducers were arithmetically averaged. Then, assuming constant

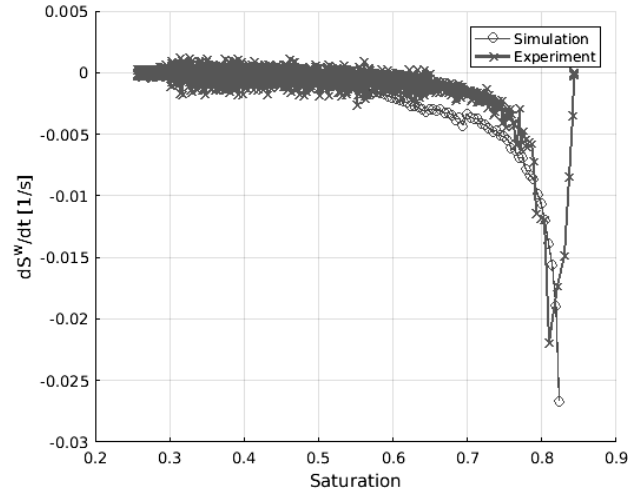


Fig. 5.6 Global  $\frac{dS^w}{dt}$  during drainage: comparison between simulation and experimental measurement

air phase pressure, pressure difference ( $P^a - P^w$ ) as a function of time was calculated. The capillary pressure-saturation relationship that was measured quasi-statically was assumed to hold under dynamic conditions. With all these experimental data, dynamic capillarity coefficient  $\tau$  could be calculated using Eq. (5.2) (see Zhuang et al. (2017)).

To calculate dynamic capillarity coefficient  $\tau$  from simulations, we also needed to observe consistency in scale. We have calculated  $\tau$  for global and local scale: namely, saturation and pressure are averaged over whole network or middle 1/3 network, respectively. Same fitted  $P^c - S^w$  by van Genuchten equation (Van Genuchten, 1980) from quasi-static experiment is adopted for both global and local calculation. Scale dependence of  $\tau$  is given in Figure 5.7. Numerical simulation gives higher  $\tau$  globally than locally, in agreement with reported numerical and experimental findings (Bottero et al., 2011; Camps-Roach et al., 2010; Das et al., 2014; Das and Mirzaei, 2012; O'Carroll et al., 2005; Sakaki et al., 2010).

**Comparison of  $\tau$  from experiment and simulations** Figure 5.8 gives  $\tau$  change with saturation from simulations and experimental measurement. Our simulation can reproduce experimental global  $\frac{dS^w}{dt}$  as in Figure 5.6. But considering issues of physical pressure upscaling from pore-scale to REV-scale (Nordbotten et al., 2007, 2008) and correspondence between measured pressure and numerical one, it is rather difficult

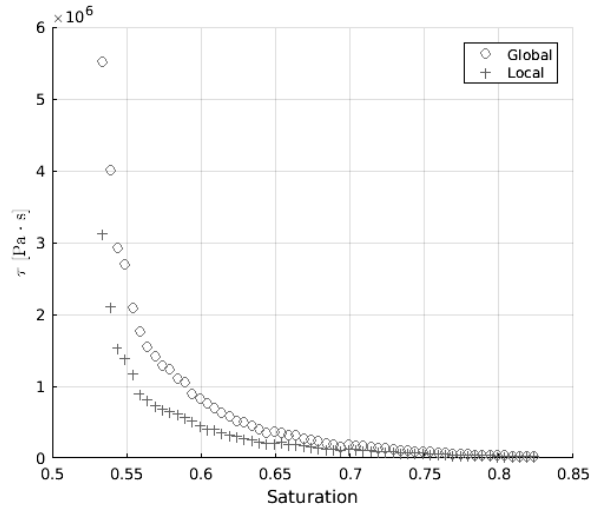


Fig. 5.7 Scale dependence of  $\tau$  from simulation

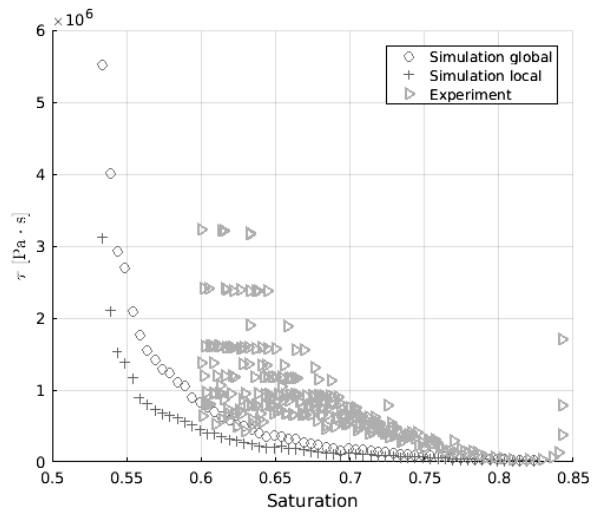


Fig. 5.8 Global  $\frac{dS^w}{dt}$  during drainage: comparison between simulation and experimental measurement

to justify pressure prediction from numerical simulation and upscaling. Nevertheless, we observe  $\tau$  in same order or magnitude from simulation and experiment. A similar trend of  $\tau$  change with saturation is shown. Given reported wide range for  $\tau$  and even some contradictory dependency of  $\tau$  on saturation, our simulation captures the system dynamics quite well.

## 5.5 Conclusion

A dynamic single-pressure pore-network model is developed and employed for sandbox experiments simulations to study dynamic capillarity effect. Network is constructed based on sand grain size distribution, porosity, intrinsic permeability and quasi-static Pc-S curve from experimental measurements. This gives good basis for dynamic simulations. Single-pressure algorithm is adopted considering significant viscosity difference between water and air. Air phase is assumed with constant and uniform pressure distribution.

Scale dependence of dynamic capillarity coefficient  $\tau$  and  $\frac{dS^w}{dt}$  are discussed through numerical simulation. Globally we have slower invasion, thus higher  $\frac{dS^w}{dt}$  and  $\tau$  than locally.

Our simulations give good prediction of global  $\frac{dS^w}{dt}$ . Values of  $\tau$  from numerical simulations are in the same order with experimental data. Also similar trend of  $\tau$  dependence on saturation is found between numerical and experimental results. Given reported wide range for  $\tau$  and even some contradictory dependency of  $\tau$  on saturation, our simulation captures the system dynamics quite well. Simulations show the capacity of our network for dynamic experiments simulations.



## Chapter 6

# Summary

Our work on pore-scale mechanisms in porous materials has been twofold: validate/benchmark Volume-of-Fluid method against experiments; develop dynamic pore-network models and employ them for various simulations.

### 6.1 Benchmarking Volume-of-Fluid method

For a simple geometry and smooth solid surface, like single capillary rise experiment, VOF simulation gave good agreement of interface position with time between simulation and experiment. But for micromodels with complex geometry and possibly rough surface, we may be able to predict the flow pattern but we cannot capture the dynamics of the process, or we failed in both flow pattern and dynamics predictions. Difference in boundary condition and initial condition, interface modeling, “pinning” of contact line and 3D effects may explain the discrepancy between simulations and experiments.

With the development of visualization techniques, more detailed pore-scale geometry can be obtained. More finer mesh is needed when employing this high resolution geometry in direct pore-scale simulation of multiphase flow, and the simulations could be computationally expensive.

### 6.2 Development of dynamic pore-network models and their applications

Several three-dimensional unstructured dynamic pore-network models have been developed.

Time step independence is discussed through two-pressure model drainage simulations. Our simulations show that time step determination based on filling/emptying time of pore bodies is a good option. Dynamic effects in average phase pressure for fluid pairs with different viscosity ratios are studied using the code as an upscaling tool. This shows our model is promising in qualitative theoretical studies.

For cases where two fluids have significant viscosity difference, viscous pressure drop in one fluid may be negligible. Two-pressure algorithm then can be replaced by a single-pressure one. Single-pressure algorithms for both drainage and imbibition are developed. Saturation patterns during imbibition for different boundary pressure drops are studied. With increase of boundary pressure, invasion becomes less capillary dominant and wetting front gets sharper.

Single-pressure imbibition model is employed for simulating of a droplet penetration into the coating layer of a coated paper. Geometry and topology of the pore network are based on FIB-SEM images of the coating material. Penetration of different sizes of droplets of different material properties into pore network of different geometries are simulated. Droplet sizes are comparable with those of real inkjet droplets. All simulations show a linear decrease of droplet volume with time, and this contradicts the expected  $\sqrt{t}$ -behavior in vertical imbibition that is obtained using single-phase Darcy's law. This discrepancy is partly due to the important effect of radial flow and partly due to the inadequacy of single-phase Darcy's law for this two-phase flow problem. The examination of saturation patterns obtained from our simulations shows that no sharp invasion front exists and there is (residual) nonwetting phase behind the front. This means that single-phase Darcy's law is not appropriate for macroscale simulation of liquid penetration under these conditions. It is expected that Richards equation would be a better choice (Bear, 1972; Markicevic and Navaz, 2010), although one needs to deal with more complex properties, like capillary pressure-saturation relationship, relative permeability, which may be difficult to measure for a thin paper.

To study dynamic capillarity effect, the single-pressure dynamic drainage pore-network model was employed for simulating sandbox experiments. Network was constructed based on sand grain size distribution, porosity, intrinsic permeability and quasi-static Pc-S curve from experimental measurements. This gives good basis for dynamic simulations. Air phase was assumed to have a constant and uniform pressure distribution. Scale dependence of dynamic capillarity coefficient  $\tau$  and  $\frac{dS^w}{dt}$  are discussed through numerical simulation. Our simulations give good prediction of global  $\frac{dS^w}{dt}$ . Values of  $\tau$  from numerical simulations have the same order of magnitude as

experimental data. Also, similar trend of  $\tau$  dependence on saturation is found between numerical and experimental results. Given reported wide range for  $\tau$  and even some contradictory dependency of  $\tau$  on saturation, our simulations captures the system dynamics quite well. Simulations show the ability of our network model for dynamic experiments simulations.

### **6.3 Recommendation**

We have demonstrated the capabilities of our models for pore-scale simulations of two-phase flow in porous materials. Direct pore-scale simulation of multiphase flow itself and its help in upscaling are promising. Yet more working regarding validation and benchmarking numerical models against well-controlled experiments is needed. Pore-network model is another option. If more pore-scale physics can be efficiently implemented and porous structures can be better reconstructed, capability and efficiency of pore-network model can be promising.



## Appendix A

# Possible Fluid Distribution Patterns during Primary Imbibition

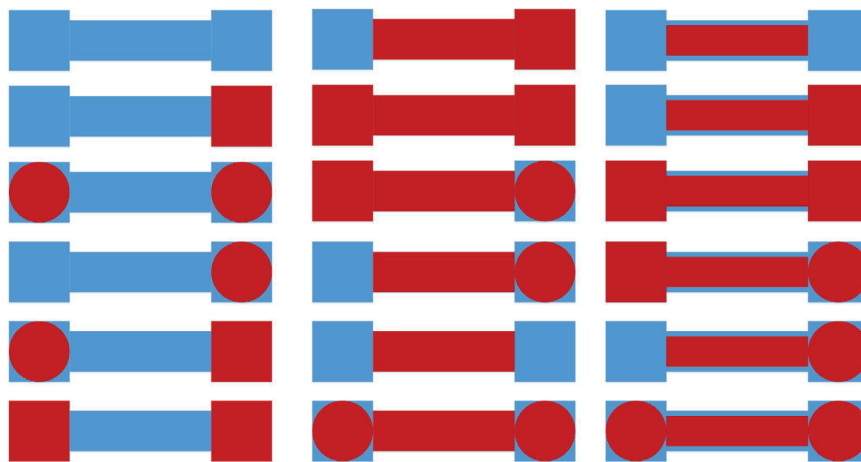


Fig. A.1 All possible liquid fillings during imbibition

In general, there are 18 possible fluid occupancy of pores, as shown in Figure A.1, where blue color shows the wetting phase and red color shows the non-wetting phase. Here, no attempt is made to represent the real interface shape. However, because of assumptions in our primary imbibition algorithm, some of these configurations will not emerge and the rest ones are shown in Figure A.2. To save computational time, we only search these liquid filling scenarios. We use A,B,C to denote three columns and

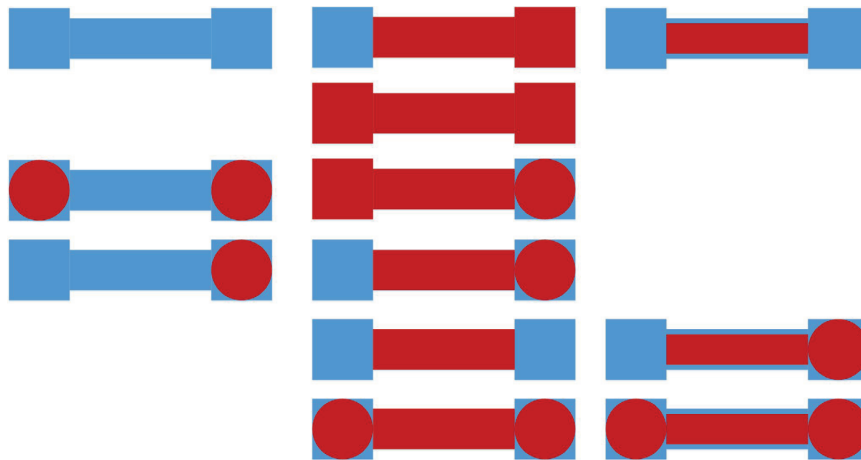


Fig. A.2 Liquid fillings during primary imbibition

1–6 to denote the six rows. So we have 18 possible distribution patterns A1 to C6 in Figure A.1. Below we explain which distribution pattern cannot be encountered and will be, therefore, excluded from considerations.

A2: As we do not consider volume of pore throats, so once there is wetting phase in the pore throat, neighboring pore body can not be still fully saturated with non-wetting phase.

A5: See A2.

A6: It is not possible to trap wetting phase during primary imbibition in our algorithm.

C2: See A2.

C3: See A6.

C4: See A2.

## Appendix B

# Interfacial Area for A Cubic Pore Body

Information of interfacial areas of corner interfaces and main terminal menisci for cubic pore bodies can be given as (Joekar-Niasar et al., 2010):

### B.1 Corner interfaces

For a pore body with inscribed radius  $R_i$  filled with wetting and non-wetting phase, non-wetting phase volume can be bigger or smaller than the inscribed sphere volume.

$$R_{i,eq} = \begin{cases} R_i \left( \frac{6}{\pi} (1 - s_i^w) \right)^{1/3} & s_i^w \geq 0.48 \\ R_i (1 - \exp(-6.83 s_i^w))^{1/3} & s_i^w < 0.48 \end{cases} \quad (\text{B.1})$$

$$A_i^{wn} = \begin{cases} 4\pi R_{i,eq}^2 & s_i^w \geq 0.48 \\ 4\pi R_{i,eq}^2 + 6\pi R_{i,eq} (R_i - R_{i,eq}) & s_i^w < 0.48 \end{cases} \quad (\text{B.2})$$

### B.2 Main terminal menisci

For main terminal meniscus, namely the interface between a pore body and its neighboring pore throat when non-wetting phase pressure in the pore body is not high enough to invade the pore throat, we have the area for this meniscus as  $8\pi \left( \frac{\sigma^{wn}}{p_i^c} \right)^2 \left( 1 - \sqrt{1 - \left( \frac{r_{ij} p_i^c}{2\sigma^{wn}} \right)^2} \right)$ .



## References

- Abidoye, L. K. and Das, D. B. (2014). Scale dependent dynamic capillary pressure effect for two-phase flow in porous media. *Advances in Water Resources*, 74:212–230.
- Aghaei, A. and Piri, M. (2015). Direct pore-to-core up-scaling of displacement processes: Dynamic pore network modeling and experimentation. *Journal of Hydrology*, 522:488–509.
- Aker, E., Måløy, K. J., Hansen, A., and Batrouni, G. G. (1998). A two-dimensional network simulator for two-phase flow in porous media. *Transport in porous media*, 32(2):163–186.
- Al-Futaisi, A. and Patzek, T. W. (2003). Extension of Hoshen–Kopelman algorithm to non-lattice environments. *Physica A: Statistical Mechanics and its Applications*, 321(3):665–678.
- Al-Gharbi, M. S. and Blunt, M. J. (2005). Dynamic network modeling of two-phase drainage in porous media. *Physical Review E*, 71(1):016308.
- Alleborn, N. and Raszillier, H. (2004). Spreading and sorption of a droplet on a porous substrate. *Chemical Engineering Science*, 59(10):2071–2088.
- Anderson, D. M. (2005). Imbibition of a liquid droplet on a deformable porous substrate. *Physics of Fluids*, 17(8):087104.
- Aslannejad, H., Hassanizadeh, S., Raoof, A., de Winter, D., Tomozeiu, N., and van Genuchten, M. (2017). Characterizing the hydraulic properties of paper coating layer using FIB-SEM tomography and 3D pore-scale modeling. *Chemical Engineering Science*, 160:275–280.
- Azzam, M. and Dullien, F. (1977). Flow in tubes with periodic step changes in diameter: A numerical solution. *Chemical Engineering Science*, 32(12):1445–1455.
- Bear, J. (1972). *Dynamics of Fluids in Porous Media*. Courier Corporation.
- Blunt, M. (2001). Flow in porous media—pore-network models and multiphase flow. *Current opinion in colloid & interface science*, 6(3):197–207.
- Blunt, M. and King, P. (1990). Macroscopic parameters from simulations of pore scale flow. *Phys. Rev. A*, 42:4780–4787.

- Blunt, M. J., Bijeljic, B., Dong, H., Gharbi, O., Iglauer, S., Mostaghimi, P., Paluszny, A., and Pentland, C. (2013). Pore-scale imaging and modelling. *Advances in Water Resources*, 51:197–216.
- Blunt, M. J. and Scher, H. (1995). Pore-level modeling of wetting. *Physical Review E*, 52(6):6387–6403.
- Bottero, S., Hassanizadeh, S. M., Kleingeld, P. J., and Heimovaara, T. J. (2011). Nonequilibrium capillarity effects in two-phase flow through porous media at different scales. *Water Resources Research*, 47(10).
- Brackbill, J., Kothe, D., and Zemach, C. (1992). A continuum method for modeling surface tension. *Journal of Computational Physics*, 100(2):335–354.
- Camps-Roach, G., O’Carroll, D. M., Newson, T. A., Sakaki, T., and Illangasekare, T. H. (2010). Experimental investigation of dynamic effects in capillary pressure: Grain size dependency and upscaling. *Water Resources Research*, 46(8).
- Clarke, A., Blake, T., Carruthers, K., and Woodward, A. (2002). Spreading and imbibition of liquid droplets on porous surfaces. *Langmuir*, 18(8):2980–2984.
- Constantinides, G. N. and Payatakes, A. C. (1996). Network simulation of steady-state two-phase flow in consolidated porous media. *AIChE Journal*, 42(2):369–382.
- Daniel, R. C. and Berg, J. C. (2006). Spreading on and penetration into thin, permeable print media: Application to ink-jet printing. *Advances in colloid and interface science*, 123:439–469.
- Das, D. B., Gill, B. S., Abidoye, L. K., and Khudaida, K. J. (2014). A numerical study of dynamic capillary pressure effect for supercritical carbon dioxide-water flow in porous domain. *AIChE Journal*, 60(12):4266–4278.
- Das, D. B. and Mirzaei, M. (2012). Dynamic effects in capillary pressure relationships for two-phase flow in porous media: Experiments and numerical analyses. *AIChE Journal*, 58(12):3891–3903.
- Davis, S. H. and Hocking, L. M. (2000). Spreading and imbibition of viscous liquid on a porous base. II. *Physics of Fluids*, 12(7):1646–1655.
- Deshpande, S. S., Anumolu, L., and Trujillo, M. F. (2012). Evaluating the performance of the two-phase flow solver interFoam. *Computational Science & Discovery*, 5(1):014016.
- Dias, M. M. and Payatakes, A. C. (1986a). Network models for two-phase flow in porous media Part 1. Immiscible microdisplacement of non-wetting fluids. *Journal of Fluid Mechanics*, 164:305–336.
- Dias, M. M. and Payatakes, A. C. (1986b). Network models for two-phase flow in porous media Part 2. Motion of oil ganglia. *Journal of Fluid Mechanics*, 164(-1):337.
- DiCarlo, D. A. (2004). Experimental measurements of saturation overshoot on infiltration. *Water Resources Research*, 40(4).

- DiCarlo, D. A. (2006). Quantitative network model predictions of saturation behind infiltration fronts and comparison with experiments. *Water Resources Research*, 42(7).
- Dullien, F. A. L. (1992). *Porous media : fluid transport and pore structure*. Academic Press.
- Ferrari, A., Jimenez-Martinez, J., Borgne, T. L., Méheust, Y., and Lunati, I. (2015). Challenges in modeling unstable two-phase flow experiments in porous micromodels. *Water Resources Research*, 51(3):1381–1400.
- Frank, X. and Perré, P. (2012). Droplet spreading on a porous surface: A lattice Boltzmann study. *Physics of Fluids*, 24(4):042101.
- Gambaryan-Roisman, T. (2014). Liquids on porous layers: Wetting, imbibition and transport processes. *Current Opinion in Colloid and Interface Science*, 19(4):320–335.
- Geiger, S. L. and Durnford, D. S. (2000). Infiltration in homogeneous sands and a mechanistic model of unstable flow. *Soil Science Society of America Journal*, 64(2):460–469.
- Hassanizadeh, S. M., Celia, M. a., and Dahle, H. K. (2002). on Unsaturated Flow. *Vadose Zone Journal*, 1:38–57.
- Hassanizadeh, S. M. and Gray, W. G. (1990). Mechanics and Thermodynamics of Multiphase Flow in Porous-Media Including Interphase Boundaries. *Advances in Water Resources*, 13(4):169–186.
- Hassanizadeh, S. M. and Gray, W. G. (1993). Thermodynamic basis of capillary pressure in porous media. *Water Resources Research*, 29(10):3389–3405.
- Heshmati, M. and Piri, M. (2014). Experimental investigation of dynamic contact angle and capillary rise in tubes with circular and noncircular cross sections. *Langmuir : the ACS journal of surfaces and colloids*, 30(47):14151–62.
- Horgue, P., Augier, F., Duru, P., Prat, M., and Quintard, M. (2013). Experimental and numerical study of two-phase flows in arrays of cylinders. *Chemical Engineering Science*, 102:335–345.
- Hou, L., Chen, L., and Kibbey, T. C. G. (2012). Dynamic capillary effects in a small-volume unsaturated porous medium: Implications of sensor response and gas pressure gradients for understanding system dependencies. *Water Resources Research*, 48(11).
- Hughes, R. and Blunt, M. (2000). Pore Scale Modeling of Rate Effects in Imbibition. *Transport in Porous Media*, 40:295–322.
- Joekar-Niasar, V. and Hassanizadeh, S. (2012a). Network modeling and its application to wicking: two-phase flow approach. In Masoodi, R. and Pillai, M., editors, *Wicking in Porous Materials: Traditional and Modern Modeling Approaches*. Taylor & Francis Inc.

- Joekar Niasar, V., Hassanizadeh, S., Pyrak-Nolte, L., and Berentsen, C. (2009). Simulating drainage and imbibition experiments in a high-porosity micromodel using an unstructured pore network model. *Water resources research*, 45(2).
- Joekar-Niasar, V. and Hassanizadeh, S. M. (2011a). Effect of fluids properties on non-equilibrium capillarity effects: Dynamic pore-network modeling. *International Journal of Multiphase Flow*, 37(2):198–214.
- Joekar-Niasar, V. and Hassanizadeh, S. M. (2011b). Specific interfacial area: The missing state variable in two-phase flow equations? *Water Resources Research*, 47(5):1–14.
- Joekar-Niasar, V. and Hassanizadeh, S. M. (2012b). Analysis of Fundamentals of Two-Phase Flow in Porous Media Using Dynamic Pore-Network Models: A Review. *Critical Reviews in Environmental Science and Technology*, 42(18):1895–1976.
- Joekar-Niasar, V., Hassanizadeh, S. M., and Dahle, H. K. (2010). Non-equilibrium effects in capillarity and interfacial area in two-phase flow: dynamic pore-network modelling. *Journal of Fluid Mechanics*, 655:38–71.
- Kaestner, A., Lehmann, E., and Stampanoni, M. (2008). Imaging and image processing in porous media research. *Advances in Water Resources*, 31(9):1174–1187.
- Karadimitriou, N. K., Hassanizadeh, S. M., Joekar-Niasar, V., and Kleingeld, P. J. (2014). Micromodel study of two-phase flow under transient conditions: Quantifying effects of specific interfacial area. *Water Resources Research*, 50(10):8125–8140.
- Karpyn, Z. T. and Piri, M. (2007). Prediction of fluid occupancy in fractures using network modeling and x-ray microtomography. I: Data conditioning and model description. *Physical Review E*, 76(1):016315.
- Kettle, J., Lamminmäki, T., and Gane, P. (2010). A review of modified surfaces for high speed inkjet coating. *Surface and Coatings Technology*, 204(12-13):2103–2109.
- Korteland, S., Bottero, S., Hassanizadeh, S. M., and Berentsen, C. W. J. (2010). What is the correct definition of average pressure? *Transport in Porous Media*, 84(1):153–175.
- Kunz, P., Zarikos, I. M., Karadimitriou, N. K., Huber, M., Nieken, U., and Hassanizadeh, S. M. (2015). Study of Multi-phase Flow in Porous Media: Comparison of SPH Simulations with Micro-model Experiments. *Transport in Porous Media*.
- Lembach, A., Roisman, I., and Tropea, C. (2011). Drop impact on porous media. In *Proceeding of ILASS–Europe 2011, 24th European Conference on Liquid Atomization and Spray Systems, Estoril, Portugal*.
- Lenormand, R., Touboul, E., and Zarcone, C. (1988). Numerical models and experiments on immiscible displacements in porous media. *Journal of Fluid Mechanics*, 189(-1):165.

- Ling, B., Bao, J., Oostrom, M., Battiato, I., and Tartakovsky, A. M. (2017). Modeling variability in porescale multiphase flow experiments. *Advances in Water Resources*, 105:29–38.
- Løvoll, G., Méheust, Y., Måløy, K. J., Aker, E., and Schmittbuhl, J. (2005). Competition of gravity, capillary and viscous forces during drainage in a two-dimensional porous medium, a pore scale study. *Energy*, 30(6):861–872.
- Markicevic, B. and Navaz, H. K. (2010). Primary and Secondary Infiltration of Wetting Liquid Sessile Droplet into Porous Medium. *Transport in Porous Media*, 85(3):953–974.
- Mason, G. and Morrow, N. R. (1991). Capillary behavior of a perfectly wetting liquid in irregular triangular tubes. *Journal of Colloid and Interface Science*, 141(1):262–274.
- Mayer, R. P. and Stowe, R. A. (1965). Mercury porosimetry—breakthrough pressure for penetration between packed spheres. *Journal of Colloid Science*, 20(8):893–911.
- Meng, S., Yang, R., Wu, J.-s., and Zhang, H. (2014). Simulation of droplet spreading on porous substrates using smoothed particle hydrodynamics. *International Journal of Heat and Mass Transfer*, 77:828–833.
- Mogensen, K. and Stenby, E. H. (1998). A Dynamic Two-Phase Pore-Scale Model of Imbibition. *Transport in Porous Media*, 32:299–327.
- Nguyen, V. H., Sheppard, A. P., Knackstedt, M. A., and Val Pinczewski, W. (2006). The effect of displacement rate on imbibition relative permeability and residual saturation. *Journal of Petroleum Science and Engineering*, 52(1-4):54–70.
- Nordbotten, J. M., Celia, M. A., Dahle, H. K., and Hassanizadeh, S. M. (2007). Interpretation of macroscale variables in Darcy’s law. *Water Resources Research*, 43(8):1–9.
- Nordbotten, J. M., Celia, M. A., Dahle, H. K., and Hassanizadeh, S. M. (2008). On the definition of macroscale pressure for multiphase flow in porous media. *Water Resources Research*, 44(6):1–8.
- Nordhaug, H., Celia, M., and Dahle, H. (2003). A pore network model for calculation of interfacial velocities. *Advances in Water Resources*, 26(10):1061–1074.
- O’Carroll, D. M., Phelan, T. J., and Abriola, L. M. (2005). Exploring dynamic effects in capillary pressure in multistep outflow experiments. *Water Resources Research*, 41(11).
- Oostrom, M., Mehmani, Y., Romero-Gomez, P., Tang, Y., Liu, H., Yoon, H., Kang, Q., Joekar-Niasar, V., Balhoff, M. T., Dewers, T., Tartakovsky, G. D., Leist, E. A., Hess, N. J., Perkins, W. A., Rakowski, C. L., Richmond, M. C., Serkowski, J. A., Werth, C. J., Valocchi, A. J., Wietsma, T. W., and Zhang, C. (2016). Pore-scale and continuum simulations of solute transport micromodel benchmark experiments. *Computational Geosciences*, 20(4):857–879.

- Oren, P.-E., Bakke, S., and Arntzen, O. (1998). Extending Predictive Capabilities to Network Models. *SPE Journal*, 3(December):324–336.
- Patzek, T. (2001). Verification of a complete pore network simulator of drainage and imbibition. *SPE Journal*, 6(2):144–156.
- Piri, M. and Blunt, M. J. (2005). Three-dimensional mixed-wet random pore-scale network modeling of two- and three-phase flow in porous media. I. Model description. *Physical Review E*, 71(2):026301.
- Piri, M. and Karpyn, Z. T. (2007). Prediction of fluid occupancy in fractures using network modeling and x-ray microtomography. II: Results. *Physical Review E*, 76(1):016316.
- Princen, H. (1970). Capillary phenomena in assemblies of parallel cylinders: III. Liquid Columns between Horizontal Parallel Cylinders. *Journal of Colloid and Interface Science*, 34(2):171–184.
- Ransohoff, T. and Radke, C. (1988). Laminar flow of a wetting liquid along the corners of a predominantly gas-occupied noncircular pore. *Journal of Colloid and Interface Science*, 121(2):392–401.
- Raouf, A. and Hassanizadeh, S. M. (2012). A new formulation for pore-network modeling of two-phase flow. *Water Resources Research*, 48(1):1–13.
- Richards, L. A. (1931). Capillary conduction of liquids through porous mediums. *Physics*, 1(5):318–333.
- Sakaki, T., O’Carroll, D. M., and Illangasekare, T. H. (2010). Direct quantification of dynamic effects in capillary pressure for drainage–wetting cycles. *Vadose Zone Journal*, 9(2).
- Singh, M. and Mohanty, K. K. (2003). Dynamic modeling of drainage through three-dimensional porous materials. *Chemical Engineering Science*, 58(1):1–18.
- Starov, V., Kosvintsev, S., Sobolev, V., Velarde, M., and Zhdanov, S. (2002). Spreading of Liquid Drops over Saturated Porous Layers. *Journal of Colloid and Interface Science*, 246(2):372–379.
- Starov, V., Zhdanov, S., Kosvintsev, S., Sobolev, V., and Velarde, M. (2003). Spreading of liquid drops over porous substrates. *Advances in Colloid and Interface Science*, 104(1):123–158.
- Thompson, K. E. (2002). Pore-scale modeling of fluid transport in disordered fibrous materials. *AIChE Journal*, 48(7):1369–1389.
- Tørå, G., Øren, P.-E., and Hansen, A. (2012). A Dynamic Network Model for Two-Phase Flow in Porous Media. *Transport in Porous Media*, 92(1):145–164.
- Valvatne, P. H. and Blunt, M. J. (2004). Predictive pore-scale modeling of two-phase flow in mixed wet media. *Water Resources Research*, 40(7).

- Valvatne, P. H., Piri, M., Lopez, X., and Blunt, M. J. (2005). Predictive Pore-Scale Modeling of Single and Multiphase Flow. *Transport in Porous Media*, 58(1-2):23–41.
- van der Marck, S. C., Matsuura, T., and Glas, J. (1997). Viscous and capillary pressures during drainage: Network simulations and experiments. *Physical Review E*, 56(5):5675–5687.
- Van Genuchten, M. T. (1980). A closed-form equation for predicting the hydraulic conductivity of unsaturated soils. *Soil science society of America journal*, 44(5):892–898.
- Vidales, A. M., Riccardo, J. L., and Zgrablich, G. (1998). Pore-level modelling of wetting on correlated porous media. *Journal of Physics D: Applied Physics*, 31(20):2861–2868.
- Weller, H. G., Tabor, G., Jasak, H., and Fureby, C. (1998). A tensorial approach to computational continuum mechanics using object-oriented techniques. *Computers in physics*, 12(6):620–631.
- Wooding, R. A. and Morel-Seytoux, H. J. (1976). Multiphase Fluid Flow Through Porous Media. *Annual Review of Fluid Mechanics*, 8(1):233–274.
- Wörner, M. (2012). Numerical modeling of multiphase flows in microfluidics and micro process engineering: a review of methods and applications. *Microfluidics and Nanofluidics*, 12(6):841–886.
- Xu, Z., Liu, H., and Valocchi, A. J. (2017). Lattice Boltzmann simulation of immiscible two-phase flow with capillary valve effect in porous media. *Water Resources Research*, 53(5):3770–3790.
- Zhmud, B., Tiberg, F., and Hallstenson, K. (2000). Dynamics of Capillary Rise. *Journal of Colloid and Interface Science*, 228(2):263–269.
- Zhou, D., Blunt, M., and Orr, F. (1997). Hydrocarbon Drainage along Corners of Noncircular Capillaries. *Journal of Colloid and Interface Science*, 187(1):11–21.
- Zhuang, L., Hassanizadeh, S., Qin, C., and de Waal, A. (2017). Experimental investigation of hysteretic dynamic capillarity effect in unsaturated flow. *Water Resources Research*.



## samenvatting

We presenteren directe simulaties van verschillende experimenten met verschillende geometrieën met behulp van de Volume-van-Vloeistof (VOF) methode. De correspondentie en stromingspatronen van de drukstroomsnelheid worden vergeleken tussen numerieke en experimentele gegevens. Voor een eenvoudige geometrie kunnen we de experimentele resultaten op bevredigende wijze reproduceren, terwijl significante meningsverschillen met het experiment worden waargenomen voor complexe geometrieën. Mogelijke redenen voor deze bevindingen worden geanalyseerd.

Er is een dynamisch rioleringsalgoritme met twee druk ontwikkeld voor een driedimensionaal ongestructureerd netwerkmodel. De impact van de tijdstap wordt besproken via drainagesimulaties. Dynamische effecten in gemiddelde fasedruk voor vloeistoffasen met verschillende viscositeitsverhoudingen worden verkend met behulp van de ontwikkelde code als opschalingshulpmiddel. Voor gevallen waarbij twee vloeistoffen aanzienlijke viscositeitsverschillen hebben, kan de viskeuze drukval binnen één vloeistof worden verwaarloosd. Dit dynamische algoritme kan verder worden vereenvoudigd tot een algoritme met één druk. Deze vereenvoudigingen zijn gedaan voor zowel drainage als imbibitie. Verzadigingspatroon tijdens imbibitie voor verschillende grensdrukdalingen worden bestudeerd. Met een toename van de grensdruk wordt invasie minder capillair dominant met een bevochtigend front. De single-pressure algoritmen voor drainage en imbibitie zijn gebruikt voor simulaties van sandbox-experimenten en vloeistofpenetratie in de papiercoatinglaag.

